THE JOURNAL OF BIOLOGICAL CHEMISTRY VOL. 290, NO. 9, pp. 5707–5724, February 27, 2015

Role of the Outer Pore Domain in Transient Receptor Potential Vanilloid 1 Dynamic Permeability to Large Cations*

Received for publication, July 16, 2014, and in revised form, December 30, 2014 Published, JBC Papers in Press, January 7, 2015, DOI 10.1074/jbc.M114.597435

Clare H. Munns[‡], Man-Kyo Chung[§], Yuly E. Sanchez[¶‖], L. Mario Amzel[¶], and Michael J. Caterina[‡1]**

*From the [‡]Departments of Neurosurgery, Biological Chemistry, and Neuroscience, Neurosurgery Pain Research Institute, and Center for Sensory Biology and [¶]Department of Biophysics and Biophysical Chemistry, Johns Hopkins School of Medicine, Baltimore, Maryland 21205, the [§]Department of Neural and Pain Sciences, University of Maryland School of Dentistry, Baltimore, Maryland 21201, the [‖]Departamento de Física, Facultad de Ciencias, Universidad Nacional de Colombia, 111321 Bogotá, D.C., Colombia, and the **Departamento de Nutrición y Bioquímica, Facultad de Ciencias, Pontificia Universidad Javeriana, 110231 Bogotá, D.C., Colombia*

Background: The TRPV1 ion channel alters its ionic selectivity in an activity-dependent manner.
Results: Mutations in multiple subregions of the TRPV1 pore selectively augment or reduce large cation permeability changes.
Conclusion: Side chain identities within the pore shape conformational changes underlying dynamic ionic selectivity.
Significance: Understanding TRPV1 dynamic ionic selectivity will provide crucial insight into channel activation and nociceptive signaling.

Transient receptor potential vanilloid 1 (TRPV1) has been shown to alter its ionic selectivity profile in a time- and agonist-dependent manner. One hallmark of this dynamic process is an increased permeability to large cations such as *N*-methyl-D-glucamine (NMDG). In this study, we mutated residues throughout the TRPV1 pore domain to identify loci that contribute to dynamic large cation permeability. Using resiniferatoxin (RTX) as the agonist, we identified multiple gain-of-function substitutions within the TRPV1 pore turret (N628P and S629A), pore helix (F638A), and selectivity filter (M644A) domains. In all of these mutants, maximum NMDG permeability was substantially greater than that recorded in wild type TRPV1, despite similar or even reduced sodium current density. Two additional mutants, located in the pore turret (G618W) and selectivity filter (M644I), resulted in significantly reduced maximum NMDG permeability. M644A and M644I also showed increased and decreased minimum NMDG permeability, respectively. The phenotypes of this panel of mutants were confirmed by imaging the RTX-evoked uptake of the large cationic fluorescent dye YO-PRO1. Whereas none of the mutations selectively altered capsaicin-induced changes in NMDG permeability, the loss-of-function phenotypes seen with RTX stimulation of G618W and M644I were recapitulated in the capsaicin-evoked YO-PRO1 uptake assay. Curiously, the M644A substitution resulted in a loss, rather than a gain, in capsaicin-evoked YO-PRO1 uptake. Modeling of our mutations onto the recently determined TRPV1 structure revealed several plausible mechanisms for the phenotypes observed. We conclude that side chain interactions at a few specific loci within the TRPV1 pore contribute to the dynamic process of ionic selectivity.

Transient receptor potential vanilloid 1 (TRPV1)[2] is an ion channel that can be gated by vanilloid compounds such as capsaicin (the spicy component of chili peppers) and resiniferatoxin (RTX) or, alternatively, by other agonists, including noxious heat (>42 °C), protons, and certain lipids (1, 2). TRPV1 is highly expressed in primary nociceptive sensory neurons, where it contributes to heat- and chemical-evoked pain. Functional TRPV1 channels consist of four identical subunits, each possessing six transmembrane (TM) domains and a pore region located between TM5 and TM6 (3, 4).

Like most TRP channels, TRPV1 is a nonselective cation channel. It exhibits similar permeabilities to sodium *versus* potassium ions but with an ~10-fold greater preference for calcium over monovalent cations and an exceptionally high permeability to large cations (5–9). A remarkable feature of TRPV1-mediated ion permeation is that its cation selectivity profile is not invariant, but rather it can change as a function of activation state (10). During prolonged activation with vanilloids, permeability to large cations, such as *N*-methyl-D-glucamine (NMDG) or the propidium dye YO-PRO1, increases, despite the channel continuing to exclude anions and regardless of whether NMDG is used as the predominant intracellular or extracellular cation. Selectivity for calcium is also altered, although the direction and magnitude of this change depend upon the extracellular calcium concentration. These dynamic permeability effects are influenced by both agonist concentra-

* This work was supported, in whole or in part, by National Institutes of Health Grant NS054902 from NINDS (to M. J. C.), Grant DE023846 from NIDCR (to M. K. C.) by funding from the Neurosurgery Pain Research Institute and Blaustein Pain Research Fund at Johns Hopkins School of Medicine (to M. J. C.), and a John J. Bonica Fellowship from the International Association for the Study of Pain (to C. H. M.). Dr. Caterina is an inventor on a patent on the use of products related to TRPV1, which is licensed through UCSF and Merck. This conflict is being managed by the Johns Hopkins Office on Policy Coordination.

[1] To whom correspondence should be addressed: Depts. of Neurosurgery, Biological Chemistry, and Neuroscience, Neurosurgery Pain Research Institute, and Center for Sensory Biology, Johns Hopkins School of Medicine, 725 N. Wolfe St., Baltimore, MD 21205. Tel.: 410-502-5457; E-mail: caterina@jhmi.edu.

[2] The abbreviations used are: TRPV1, transient receptor potential vanilloid 1; NMDG, *N*-methyl-D-glucamine; RTX, resiniferatoxin; TM, transmembrane; E_{rev}, reversal potential; P_{NMDG}/P_{Na}, NMDG permeability relative to sodium; DkTx, double knot toxin; rTRPV1, rat TRPV1; mTRPV1, mouse TRPV1.

tion and agonist identity. High concentrations of capsaicin readily evoke a robust increase in large cation permeability, whereas low concentrations normally do not, unless TRPV1 has been phosphorylated by PKC. Moreover, certain agonists, such as camphor and heat, evoke only minimal changes in large cation permeability.

Agonist-evoked changes in ionic selectivity are not restricted to TRPV1 but have additionally been reported for TRPV3 and TRPA1 (11–14). Outside of the TRP channel family, ATP-gated P2X channels also show increased permeability to large cations following prolonged activation (15–18). Two distinct mechanisms have been proposed for P2X-mediated large cation uptake as follows: agonist-evoked conformational changes within the P2X channel pore itself and activity-induced recruitment of a separate large pore hemichannel (19, 20). In the case of TRPV1, current data suggest that large cations are taken up via the channel pore (10), although the nature of any conformational changes associated with this uptake is unknown.

In this study, we hypothesized that introducing mutations into the TRPV1 outer pore region would perturb the ability of the channel to alter its selectivity profile. We therefore systematically mutated the TRPV1 pore in an attempt to gain insight into the mechanisms underlying vanilloid-induced increases in large cation permeability. This strategy yielded both gain- and loss-of-function mutants, allowing us to identify several loci within the pore turret, pore helix, and selectivity filter domains that influence this activity-dependent process.

EXPERIMENTAL PROCEDURES

Chemicals—All chemical reagents were obtained from Sigma, unless otherwise specified. RTX and capsaicin were dissolved in ethanol and YO-PRO1 iodide (Invitrogen) in DMSO. All reagents were diluted in aqueous solution on the day of the experiment.

Site-directed Mutagenesis and Cell Culture—Rat and mouse TRPV1 cDNAs, subcloned into pcDNA3, have been previously described (1, 11). Residue-specific mutations were introduced into these cDNAs using the QuikChange mutagenesis kit (Stratagene) and sequence-confirmed. Most mutants containing substitutions at rTRPV1-N628 for use in electrophysiology experiments were subcloned into pcDNA5 (21). rTRPV1-N628P was also generated in pcDNA3 for use in YO-PRO1 uptake experiments. HEK293 cells were transiently transfected with 1 μg of plasmid encoding wild type or mutant TRPV1, along with a separate plasmid encoding the fluorescent marker mCherry, using PolyJet DNA transfection reagent (SignaGen). All experiments were performed 1 day after transfection.

Electrophysiology—Whole cell voltage clamp was used to monitor agonist-evoked changes in ionic selectivity as described (10). Transfected HEK293 cells were bathed in extracellular solution containing (in mM) the following: 140 NaCl, 4 KCl, 2 $CaCl_2$, 2 $MgCl_2$, 10 HEPES, 5 glucose, adjusted to pH 7.4 with NaOH. Borosilicate glass electrodes were pulled to a resistance of 2–5 megaohms on a P-97 Flaming/Brown micropipette puller (Sutter) and were filled with internal solution containing (in mM) the following: 150 NaOH, 10 EDTA, 10 HEPES, adjusted to pH 7.4 with HCl. Once the whole cell mode had been reached, the extracellular solution was exchanged to one containing 150 mM NMDG, 10 mM EDTA, 10 mM HEPES, adjusted to pH 7.4 with HCl, to allow evaluation of P_{NMDG}/P_{Na}. Osmolarity of all solutions was adjusted to 290 ± 10 mosM with mannitol. Holding potential was set to 0 mV, and series resistance was compensated by >70%. Voltage ramps (1 mV ms^{-1}, 0.5 Hz) were applied as cells were stimulated with varying concentrations of RTX and capsaicin, delivered via a gravity-driven application system at a flow rate of 3 ml/min into a bath of ~200 μl (10). To account for delays in agonist delivery, kinetic measurements on responses were performed only once the current-voltage traces rose above baseline. Agonist-evoked currents were recorded using an Axopatch 200B amplifier and pClamp 9 software (Molecular Devices).

Relative ionic permeabilities were determined as described previously (10). Reversal potential (E_{rev}) was monitored throughout agonist application and was corrected for liquid junction potential (range 2.1 to 3.5 mV, calculated using pClamp software) prior to the calculation of P_{NMDG}/P_{Na} using Equation 1,

$$\frac{P_{NMDG}}{P_{Na}} = \frac{[NMDG^+]_0}{[Na+]_0} \times e^{\frac{\Delta E_{rev} F}{RT}} \quad \text{(Eq. 1)}$$

where F is the Faraday constant; R is the gas constant; T is absolute temperature (297.15 K, room temperature); ΔE_{rev} is the difference in reversal potential between extracellular $NMDG^+$ and Na^+ ions, and $[X^+]$ is the activity of ion X^+. The activity coefficients used for calculating $[X^+]$ are 0.75 for Na^+ and 0.81 for $NMDG^+$. The subscript *o* represents extracellular. In agreement with previous findings, E_{rev} in the presence of external Na^+ was close to 0 mV (range −2 to −3.9 mV) when recorded from cells expressing either WT rTRPV1 or one of four selected pore mutants (G618W, N628P, M644A, and M644I) (10), and therefore an E_{Na} value of 0 mV was used for all NMDG permeability calculations. Inclusion of actual mean E_{Na} values did not substantially alter the NMDG permeability phenotypes of these mutants.

To ensure that any observed alterations in ionic selectivity in pore mutants were not due to global changes in channel function, this latter parameter was assayed in two ways. We recorded peak outward sodium current density measured at +20 mV, as well as sodium conductance calculated using Equation 2,

$$g = \frac{i}{(E_m - E_{rev})} \quad \text{(Eq. 2)}$$

where g is conductance; i is current amplitude, and $E_m = E_{rev} + 10$ mV.

YO-PRO1 Uptake Assay—HEK293 cells expressing TRPV1 plus mCherry were bathed in extracellular solution containing (in mM) the following: 150 NaOH, 10 EDTA, 10 HEPES, adjusted to pH 7.4 with HCl. YO-PRO1 (1 μM) was added to the perfusate for 60 s before the addition of RTX or capsaicin, in the continued presence of the dye. Flow rate was ~1.5 ml/min. Fluorescence intensity (470 nm excitation, 525 nm emission, measured every 2 s) was recorded in individual cells and visualized on an inverted microscope (Nikon), using a CCD camera (Coolsnap ES, Roper) and Ratiotool software (ISee Imaging). Control cells were transfected with empty pcDNA3 plasmid

plus mCherry. Rates of change in YO-PRO1 fluorescence at each 2-s interval were averaged across all mCherry-positive cells on a coverslip (identified without visualizing YO-PRO1 fluorescence) and normalized to the average peak rate recorded from wild type coverslips on that same day.

Immunoblot Analysis—HEK293 cells transfected with wild type or mutant TRPV1 were lysed using mammalian protein extraction reagent (Pierce), supplemented with a mixture of protease inhibitors (in μg/ml: 1 leupeptin, 2 antipain, 10 aprotinin, 10 benzamidine, 1 chymostatin, 1 pepstatin-A). Protein concentration of lysates was measured using the bicinchoninic acid method (Pierce). Equal amounts of protein from parallel lysates were subjected to PAGE on 7.5% gels (TGX^{TM}, Bio-Rad) and transferred to polyvinylidine difluoride membranes. Blots were blocked in 5% bovine serum albumin in TBST (20 mM Tris, 150 mM NaCl, 0.05% Tween 20, pH 7.2), probed with rabbit anti-TRPV1 (1:1000) (22) or mouse anti-actin (1:1000, Sigma), washed in TBST, probed with horseradish peroxidase-conjugated goat anti-rabbit IgG (1:5000, Amersham Biosciences) or horseradish peroxidase-conjugated goat anti-mouse IgG (1:2000, Jackson ImmunoResearch), washed with TBST, subjected to enhanced chemiluminescence (GE Healthcare), and exposed to photographic film. Films were scanned on a flatbed scanner and analyzed by densitometry using ImageJ software (National Institutes of Health). The intensity of the TRPV1 band for each sample was normalized to actin, and this ratio, in turn, was normalized to the average value for wild type TRPV1 samples transfected on the same day. Data from three to four independent transfections for each construct were averaged to obtain the value used for normalization of YO-PRO1 uptake rates.

Structural Modeling—Structural modeling of TRPV1 substitutions was performed using the published structures of apo-TRPV1 (Protein Data Bank code 3J5P) capsaicin-bound TRPV1 (3J5R) and RTX/DkTx-bound TRPV1 (3J5Q) as templates (3, 4). To prepare Protein Data Bank structures for energy minimization, histidine residues were converted to protonated histidine, and several glutamates with missing atoms beyond Cβ (Glu-361, Glu-391, and Glu-397) were converted to alanine. Wild type structural models were energy-minimized using CHARMM (23). Backbone structural changes were constrained by applying an energetic penalty of 1 kcal/mol Å^2 to the Cα. Using Mac PyMOL (Schrödinger), mutant substitutions were introduced individually into the resulting structural models, and energy minimization was repeated using the same parameters.

Statistical Analysis—Mutant channels were compared against wild type TRPV1 using two-tailed unpaired Student's *t* test or Kaplan-Meier test. A p value of < 0.05 was considered statistically significant.

RESULTS

Mutations in the TRPV1 Outer Pore Domain Alter Dynamic Ionic Selectivity—Dynamic ionic selectivity in recombinant TRPV1 channels was initially assessed by looking for changes in permeability to the large monovalent cation NMDG. Under voltage clamp conditions, and with NMDG and sodium as the sole external and internal cations, respectively, whole cell currents were recorded from HEK293 cells expressing wild type (WT) rat TRPV1 (rTRPV1) or mouse TRPV1 (mTRPV1). Application of the TRPV1 agonist RTX (1 μM) produced a large outward sodium current at +20 mV that reached a peak with a time constant of 3.5 ± 0.1 s (mean ± S.E.) before declining to a much lower plateau (Fig. 1, *A* and *B*). In contrast, inward NMDG current recorded at −100 mV rose more slowly, with a time constant of 15.7 ± 1.1 s in rat TRPV1 and 12.2 ± 1 s in mouse TRPV1 ($p < 0.001$ *versus* rise in outward sodium current). Consequently, at the time of the sodium current peak, the inward NMDG current recorded at −100 mV had reached only 34.3 ± 1.7% (rat) or 38.4 ± 2% (mouse) of its eventual maximum. Current at −60 mV consisted of a transient outward sodium phase followed by a sustained inward NMDG component. Like the sodium current rise, the sodium current decline observed at +20 mV was rapid (with a time constant of 3.4 ± 0.5 s in rat and 2.9 ± 0.3 s in mouse), relative to the rise in NMDG current (Figs. 1, *A* and *B*, and 2*A*), and did not occur when sodium was used as both the intracellular and extracellular cation (data not shown) (10). One likely contributor to the time-dependent sodium current decline is a progressive increase in TRPV1 relative permeability to NMDG, such that inward NMDG current begins to negate the outward sodium current. We cannot exclude a contribution from other processes, such as NMDG ions entering the pore and blocking outward sodium flux. However, any such block is likely limited in extent, because the sodium current conductance, measured as the slope of the outward current within 10 mV of the reversal potential (E_{rev}) of the RTX-evoked current, declined by only ~10–15% from its initial peak in rTRPV1 (Fig. 2*B*).

As reported previously (10), the E_{rev} of the RTX-evoked current exhibited by WT rTRPV1 gradually shifted from −77.4 ± 0.6 to −34.6 ± 1 mV ($p < 0.001$, $n = 98$). According to Equation 1 (see under "Experimental Procedures"), this corresponded to an increase in the apparent permeability of NMDG relative to sodium (P_{NMDG}/P_{Na}), from a minimum of 0.05 ± 0.002 at the onset of continuous RTX stimulation to a maximum of 0.3 ± 0.01 ($p < 0.001$) (Figs. 1*A* and 2*C*). As with NMDG current, much of this increase in relative NMDG permeability occurred following the peak of the outward sodium current. At the time of this peak, P_{NMDG}/P_{Na} had increased to just 9.6 ± 0.8% of its maximum. Thirty seconds post-peak, sodium current had plateaued at 25.2 ± 1.3% of peak, and NMDG current was continuing to climb, reaching 81.2 ± 1.1% of its maximum, and P_{NMDG}/P_{Na} had increased to 77.4 ± 1.2% of its maximum. Consequently, both NMDG current and P_{NMDG}/P_{Na} reached their maxima after sodium current amplitude had ceased to change measurably (Figs. 1*A* and 2*A*).

A similar dynamic pattern of ionic selectivity was recorded in WT mTRPV1, whose E_{rev} shifted from −75.1 ± 0.8 to −34.2 ± 1.2 mV ($p < 0.001$, $n = 81$), corresponding to an ~5-fold increase in P_{NMDG}/P_{Na} from 0.06 ± 0.002 to 0.3 ± 0.01 ($p < 0.001$) (Figs. 1*B* and 2*E*). The RTX-evoked change in NMDG permeability ($\Delta P_{NMDG}/P_{Na}$) did not differ between species (0.25 ± 0.01 in rTRPV1 *versus* 0.25 ± 0.01 in mTRPV1). The rate of change in E_{rev} was also comparable between rat and mouse channels (rTRPV1, $\tau = 10.5 \pm 0.6$ s; mTRPV1, $\tau = 10 \pm 0.7$ s), and in each case it was slower than the rate of change in

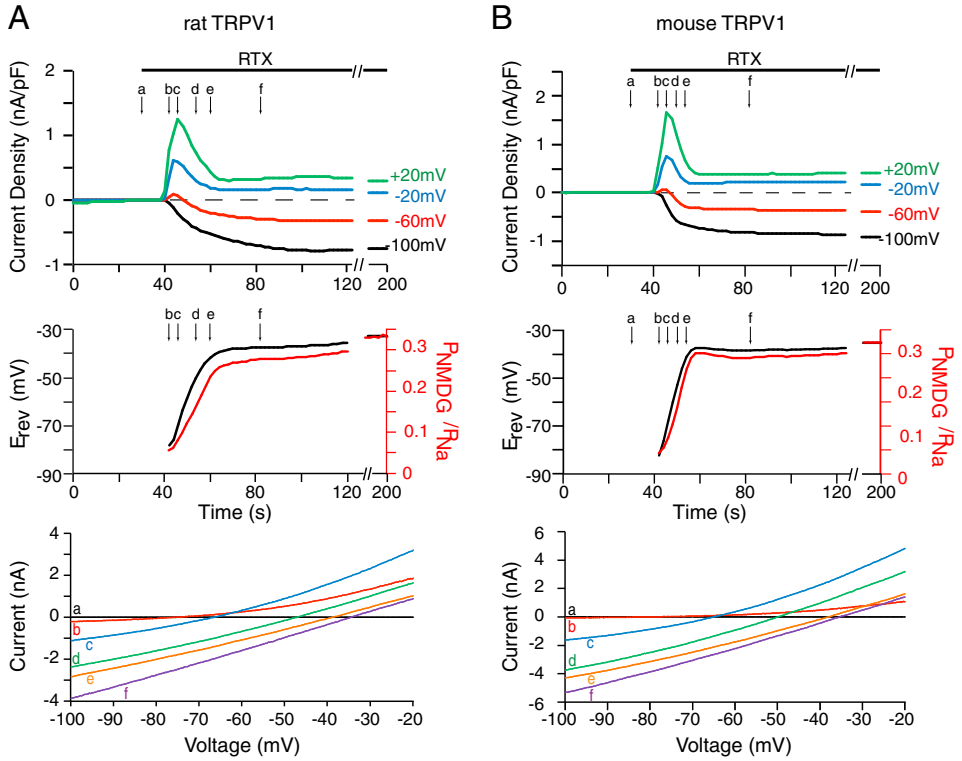

FIGURE 1. **RTX-evoked increase in NMDG permeability via wild type TRPV1 channels.** *A* and *B*, representative traces of RTX (1 μM)-evoked currents recorded from HEK293 cells transfected with wild type rat (*A*) or mouse (*B*) TRPV1. *Top*, whole cell current density recorded in the presence of 150 mM intracellular sodium and 150 mM extracellular NMDG. *Middle*, corresponding shifts in reversal potential (E_{rev}, *black trace*) and NMDG permeability (P_{NMDG}/P_{Na}, *red trace*). *Bottom*, current-voltage (*IV*) curves extracted at the indicated time points.

the outward sodium current, measured at +20 mV (Fig. 2, *D* and *F*). The relationship between peak sodium current density and change in NMDG permeability was not linear (Fig. 2, *G* and *H*). For any given range of sodium current densities, there was significant variability in the RTX-evoked $\Delta P_{NMDG}/P_{Na}$. Furthermore, there was no overall correlation between peak sodium current density and minimum or maximum NMDG permeability (data not shown). A lack of correlation between outward current density and P_{NMDG}/P_{Na} has previously been reported for $P2X_2$ channels (24, 25). As suggested in those studies, current density-independent variability in ionic selectivity changes could be due to biological differences between cell batches used for channel recording. For example, changes within the channel pore giving rise to altered ionic selectivity might be influenced by components of the surrounding membrane and/or cytosol that differ between cells. Nevertheless, despite such variability, in mouse TRPV1, peak outward sodium current densities of less than 1 nA/picofarad were typically associated with lower RTX-evoked $\Delta P_{NMDG}/P_{Na}$ (correlation coefficient, $r = 0.6$). In rat TRPV1, any such correlation was less clear.

The outer pore of TRPV1 is created by the loop between TM5 and TM6 and consists of adjoined pore helix and selectivity filter domains, flanked by pore turret domains (3, 4, 26). Given its importance in defining ion selectivity, we hypothesized that introducing mutations into the TRPV1 outer pore region would perturb the ability of the channel to alter its selectivity profile, and consequently, we undertook a series of scanning mutagenesis experiments that spanned the region from the large pore turret distal to TM5, through the pore helix, and into the selectivity filter. We first assessed 19 alanine substitution mutants for RTX-evoked $\Delta P_{NMDG}/P_{Na}$. To avoid over-interpretation of $\Delta P_{NMDG}/P_{Na}$ deficits in mutant channels that might exhibit more general functional impairments and to account for potential current density dependence of dynamic NMDG permeability, we also compared the sizes of sodium currents measured at +20 mV. Two mutants were nonfunctional (L637A and K639A), and three were severely hypofunctional (L630A, F640A, and G645A) based on sodium current density, precluding accurate E_{rev} measurement. Of the remaining 14 mutants, two were statistically indistinguishable from WT TRPV1 in terms of peak sodium current density and minimal, maximal, and $\Delta P_{NMDG}/P_{Na}$ (Y631A and T633A) (Fig. 3*A*). Nine mutants showed a reduction in RTX-evoked $\Delta P_{NMDG}/P_{Na}$ but also exhibited substantially smaller sodium currents (Fig. 3*C*). We therefore could not classify these latter mutants as having a selective loss-of-function in terms of large cation permeability. The final three mutants, S629A (located in the pore turret just above the pore helix), F638A (located in the pore helix), and M644A (located in the selectivity filter), all displayed a gain-of-function phenotype. Although their peak sodium current densities were slightly smaller than that of WT rTRPV1, the RTX-evoked $\Delta P_{NMDG}/P_{Na}$ values were significantly increased (0.37 ± 0.03 in S629A ($p < 0.001$, $n = 18$); 0.41 ± 0.03 in F638A ($p < 0.001$, $n = 13$); and 0.63 ± 0.04 in M644A ($p < 0.001$, $n = 16$); compared with 0.25 ± 0.01 in WT rTRPV1) (Fig. 3*A*; Table 1). The disproportionate increase in NMDG permeability was clearly evident when $\Delta P_{NMDG}/P_{Na}$ was plotted

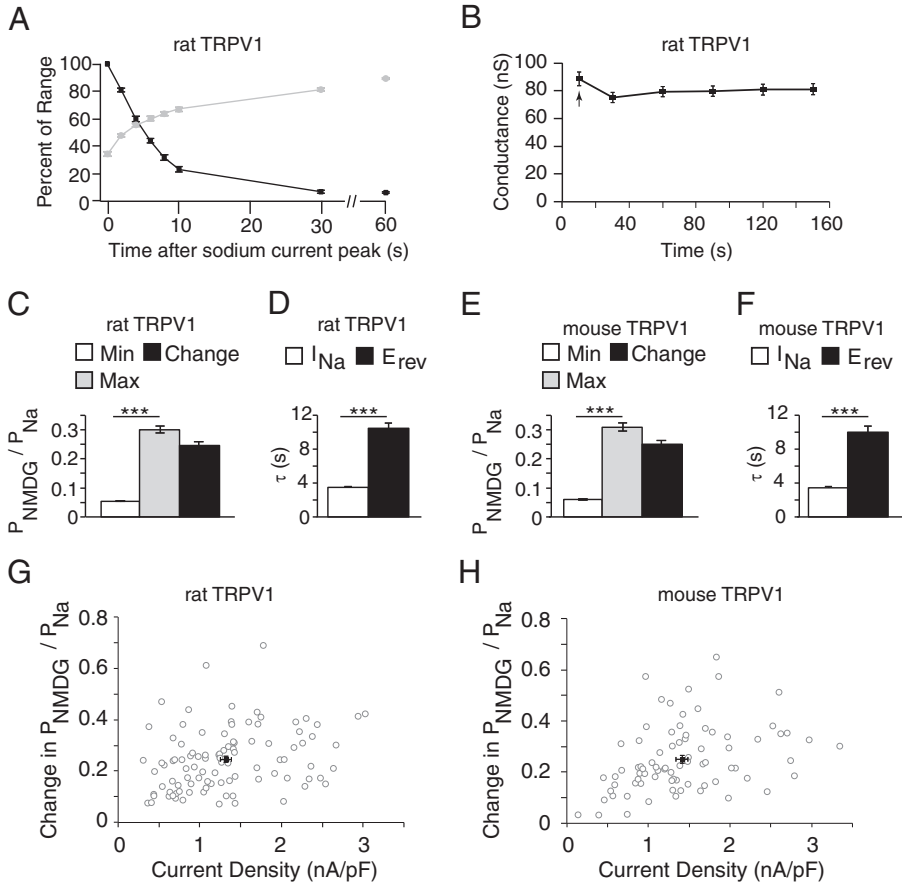

FIGURE 2. **Analysis of RTX-induced cation permeability changes in TRPV1.** *A,* summarized change in rat TRPV1-mediated RTX-evoked sodium current at +20 mV (*black symbols*) and NMDG current at −100 mV (*gray symbols*) after the point of maximal sodium current in the experiment shown in Fig. 1. Data are normalized to the maximal currents observed for either ion and are presented as mean ± S.E., $n = 98$. *B,* time-dependent changes in sodium conductance (measured between E_{rev} and E_{rev} + 10 mV) in rat TRPV1 during stimulation with RTX as in Fig. 1. Conductance plotted at 10 s (*arrow*) is the peak value during the first 10 s of the response. Other values were measured at the indicated time points. Data are presented as mean ± S.E., $n = 98$. *C–F,* NMDG permeability and kinetic parameters measured in wild type rat (*C* and *D*, $n = 98$) and mouse (*E* and *F*, $n = 81$) TRPV1 during stimulation with RTX as in Fig. 1. *C* and *E* show values for minimum (*Min*), maximum (*Max*), and change in P_{NMDG}/P_{Na}. *D* and *F* show time constants for peak outward sodium current measured at +20 mV and rate of RTX-evoked change in E_{rev}. Data are presented as mean ± S.E. ***, $p < 0.001$ (paired Student's *t* test). *G* and *H,* change in P_{NMDG}/P_{Na} plotted as a function of peak sodium current density for wild type rat (*G*) and mouse (*H*) TRPV1. *Open symbols* represent individual cells, and the *filled symbol* represents the population mean. *Error bars* represent S.E.

against sodium current density, both for individual cells expressing a given mutant and for data averaged among all cells expressing a given mutant (Fig. 3*C*, data not shown). This gain-of-function was due primarily to the mutant channels reaching a greater maximum P_{NMDG}/P_{Na} during RTX stimulation, with minimum P_{NMDG}/P_{Na} values similar to or only slightly greater than that of WT TRPV1 (Fig. 3*A*).

We next postulated that introducing cysteine residues into the TRPV1 pore could hinder activity-evoked conformational changes within the channel, due either to alterations in side chain size or charge or to spontaneous formation of disulfide bonds between neighboring side chains. Of 14 mutant channels tested, 10 produced currents with measurable E_{rev} (Fig. 3*B*). Of the remaining four mutants, one was nonfunctional (L630C) and three had currents too small to enable accurate E_{rev} measurement (L635C, G643C, and D646C). With the exception of Y627C and S632C, which resembled WT rTRPV1, many of the cysteine substitutions did significantly attenuate the RTX-evoked $\Delta P_{NMDG}/P_{Na}$ (Fig. 3*B*). This was predominantly attributable to a decrease in the maximal P_{NMDG}/P_{Na} achieved. However, these same mutants also displayed a significantly smaller peak sodium current density, and thus could not be considered to be disproportionately defective in NMDG permeability dynamics (Fig. 3*C*). Thus, substitution of cysteine at these residues did not selectively alter ionic permeability.

We next tested the effects of substituting a bulky tryptophan residue in the pore helix and adjacent upper pore turret region. The selectivity filter was spared in this scan to avoid dramatic changes in pore architecture. Furthermore, although our alanine and cysteine scans were performed in rTRPV1, our tryptophan scan was performed in mTRPV1, whose amino acid sequence within the mutated region is identical to that in rat. Of 24 tryptophan mutants assayed, one (L638W) failed to respond to RTX. The remaining mutants conformed largely to the wild type phenotype, with three notable exceptions (Fig. 4, *A* and *B*). The first of these, N629W, is located within the pore turret, adjacent to the homolog of rTRPV1 Ser-629. Like rat S629A, the mouse N629W substitution enhanced the RTX-induced change in NMDG permeability 2-fold, without altering sodium current density. Tryptophan substitution at Leu-636, located in the middle of the pore helix, produced a similar effect ($\Delta P_{NMDG}/P_{Na}$, 0.5 ± 0.04 in N629W ($p < 0.001$, $n = 33$); 0.47 ±

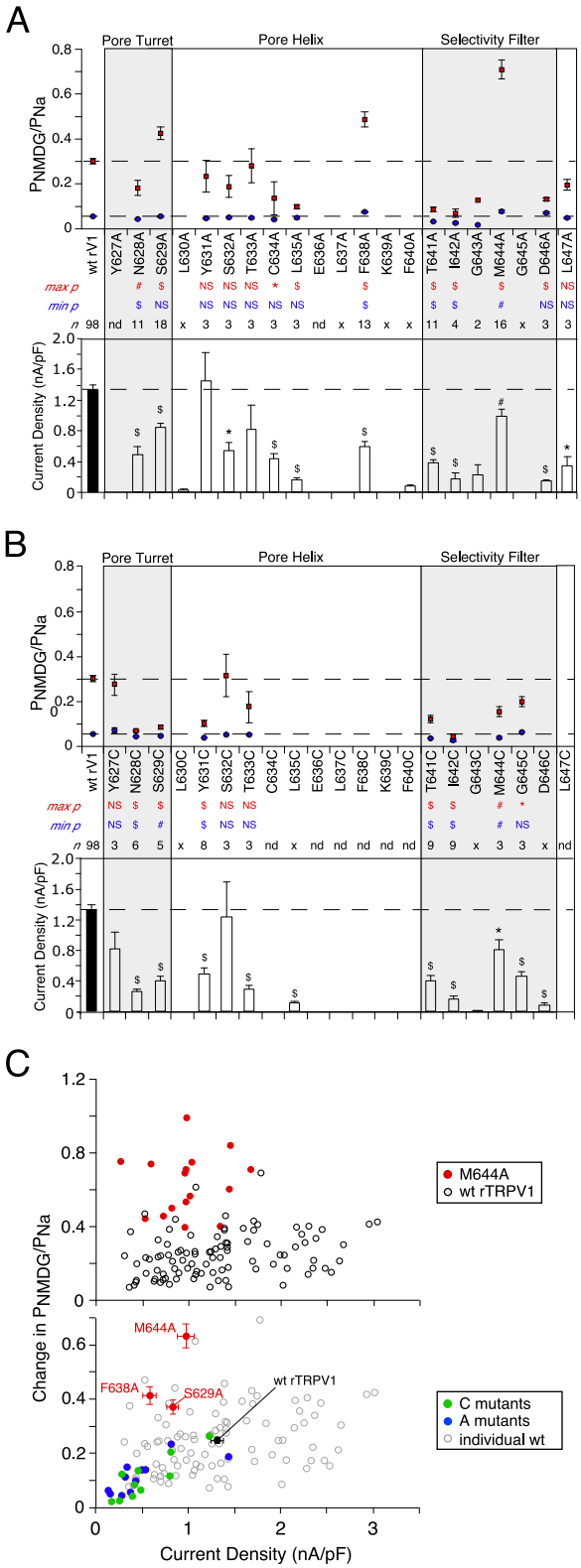

FIGURE 3. **Ionic selectivity changes following alanine or cysteine scanning mutagenesis within the outer pore region of TRPV1.** *A* and *B*, summary of alanine (*A*) and cysteine (*B*) scanning data. *Top,* minimum (*blue symbols*) and maximum (*red symbols*) P_{NMDG}/P_{Na} evoked by 1 μM RTX. *Bottom,* peak sodium current density measured at +20 mV. *Dashed lines* indicate wild type values. Data are presented as mean ± S.E. *max p*, *p* values comparing maximum P_{NMDG}/P_{Na} in wild type *versus* mutant; *min p*, *p* values comparing minimum P_{NMDG}/P_{Na} in wild type *versus* mutant; *, $p < 0.05$; #, $p < 0.01$; $, $p < 0.001$; *NS,* not statistically significant (unpaired Student's *t* test). Regions of the pore, as annotated *above* the panel, are delineated by *shading*. *n*, number of observations; *nd,* not determined; *x,* E_{rev} not measurable. *C,* change in P_{NMDG}/P_{Na} plotted as a function of peak sodium current density for wild type and mutant TRPV1. *Top,* individual recordings from cells expressing wild type rat TRPV1 (*open symbols*) or rTRPV1-M644A (*red symbols*). *Bottom,* cysteine (*green*) and alanine (*blue*) mutant populations. *Open symbols* represent individual wild type recordings. *Colored symbols* represent population means for wild type (*black*) and mutant channels. Mutants displaying a selective gain-of-function are shown in *red*. *Error bars* represent S.E. Wild type data are reproduced from Fig. 1.

0.03 in L636W ($p < 0.001$, $n = 14$); *versus* 0.25 ± 0.01 in WT mTRPV1). As with the rat TRPV1 gain-of-function mutants described above, the increased $\Delta P_{NMDG}/P_{Na}$ exhibited by these two tryptophan mutants was attributable primarily to increased maximum NMDG permeability (Fig. 4*A*; Table 1). The third mutant of interest was G619W, located in the upper pore turret, in which the maximum P_{NMDG}/P_{Na} was significantly lower than that observed in wild type TRPV1, leading to a reduced $\Delta P_{NMDG}/P_{Na}$ of 0.15 ± 0.02 ($n = 6$) in the context of a normal RTX-evoked sodium current density (Fig. 4*A*; Table 1). A nearby mutant, K616W, also trended toward reduced maximum and $\Delta P_{NMDG}/P_{Na}$ while retaining normal sodium current density, but the deviation from wild type did not reach statistical significance. Once again, plotting $\Delta P_{NMDG}/P_{Na}$ against sodium current density clearly demonstrated the disproportionate shift in ionic selectivity *versus* channel function, in both the gain- and loss-of-function mutants (Fig. 4*B*). Thus, tryptophan substitution can produce selective augmentation or impairment of dynamic large cation permeability, depending on the targeted residue.

Because two of the most robust gain-of-function phenotypes were observed in rTRPV1-M644A and mTRPV1-N629W, these two residues were subsequently chosen for further mutagenesis. First, we took advantage of an existing set of substitution mutants at the Asn-628 residue in rat TRPV1, which is homologous to mouse Asn-629 (21). Consistent with the mouse N629W mutant, substituting tryptophan for asparagine at the same position in rTRPV1 appeared to augment NMDG permeability, although the difference between mutant and wild type was not statistically significant ($\Delta P_{NMDG}/P_{Na}$, 0.34 ± 0.08 in N628W ($n = 10$) *versus* 0.25 ± 0.01 in WT rTRPV1) (Fig. 5, *A* and *B*; Table 1). The screen did, however, identify two mutations that produced a much stronger phenotype than that of the tryptophan substitution. Replacement of Asn-628 with either arginine or proline significantly increased RTX-induced $\Delta P_{NMDG}/P_{Na}$ (0.39 ± 0.04 in N628R ($p < 0.001$ *versus* WT rTRPV1, $n = 9$); 0.45 ± 0.04 in N628P ($p < 0.001$, $n = 14$)) without increasing sodium current density (Fig. 5, *A* and *B*; Table 1). As with the gain-of-function mutants described above, minimum NMDG permeability remained relatively stable, whereas maximum NMDG permeability was greatly increased (Fig. 5*A*).

Met-644 lies near the narrowest part of the open TRPV1 pore, at the center of the selectivity filter (3). Because the introduction of an alanine residue at this position appeared to augment the RTX-evoked increase in rTRPV1 large cation permeability, we hypothesized that the inclusion of larger amino acids would conversely constrict the pore, reducing minimal and/or maximal P_{NMDG}/P_{Na}. A number of mutations, including the methionine-to-alanine substitution, were therefore made at the

TABLE 1

Gain- and loss-of-function phenotypes are conserved across species

Data are presented as mean ± S.E. Min is minimum and Max is maximum.

Mutant	Min E_{rev}	Max E_{rev}	ΔE_{rev}	Min P_{NMDG}/P_{Na}	Max P_{NMDG}/P_{Na}	$\Delta P_{NMDG}/P_{Na}$	*n*
	mV	*mV*	*mV*				
Rat							
WT	−77.4 ± 0.6	−34.6 ± 1	42.8 ± 1.2	0.05 ± 0.002	0.3 ± 0.012	0.25 ± 0.012	98
G618W	−79.5 ± 2.8	−45.3 ± 3.1[a]	34.2 ± 3.7[b]	0.05 ± 0.007	0.19 ± 0.017[c]	0.14 ± 0.017[c]	9
M644I	−91.5 ± 1.7[c]	−45.2 ± 1.6[c]	46.3 ± 2.8	0.03 ± 0.002[c]	0.19 ± 0.012[c]	0.16 ± 0.013[c]	8
N628W	−76.1 ± 1.5	−29.1 ± 4.4	47 ± 4.1	0.06 ± 0.003	0.4 ± 0.08	0.34 ± 0.078	10
N628P	−76.6 ± 1.2	−20.6 ± 2.2[c]	−56 ± 2.6[c]	0.06 ± 0.003	0.5 ± 0.036[c]	0.45 ± 0.037[c]	14
F638A	−68.7 ± 1[c]	−21.3 ± 2[c]	47.4 ± 2	0.07 ± 0.003[c]	0.49 ± 0.033[c]	0.41 ± 0.032[c]	13
M644A	−68.7 ± 1.9[c]	−11.5 ± 1.6[c]	57.2 ± 2.4[c]	0.08 ± 0.006[a]	0.71 ± 0.042[c]	0.63 ± 0.042[c]	16
Mouse							
WT	−75.1 ± 0.8	−34.2 ± 1.2	40.9 ± 1.5	0.06 ± 0.002	0.31 ± 0.014	0.25 ± 0.015	81
G619W	−82.4 ± 1.9[b]	−45 ± 2.7[b]	37.3 ± 4.3	0.04 ± 0.004	0.19 ± 0.02[c]	0.15 ± 0.023	6
M645I	−86 ± 2.4[c]	−39.9 ± 2.5	46 ± 4.2	0.04 ± 0.004[a]	0.24 ± 0.027	0.2 ± 0.029	9
N629W	−71.4 ± 1.5[b]	−18.8 ± 2.1[c]	52.6 ± 2.3[c]	0.07 ± 0.005[b]	0.57 ± 0.041[c]	0.5 ± 0.041[c]	33
N629P	−75.5 ± 1.4	−26.7 ± 2.1[b]	48.8 ± 1.9[a]	0.06 ± 0.003	0.4 ± 0.031[b]	0.34 ± 0.03[b]	14
F639A	−69.8 ± 1.4[b]	−24.5 ± 3.1[a]	45.3 ± 3	0.07 ± 0.004[b]	0.44 ± 0.044[a]	0.37 ± 0.044[a]	11
M645A	−70.4 ± 2.3	−20.4 ± 3[a]	50 ± 4.3	0.07 ± 0.006	0.51 ± 0.063[c]	0.44 ± 0.066[c]	8

[a] $p < 0.01$.
[b] $p < 0.05$.
[c] $p < 0.001$ (mutant *versus* wild type, unpaired Student's *t* test). Some data are represented in graphic form in Figs. 1–6.

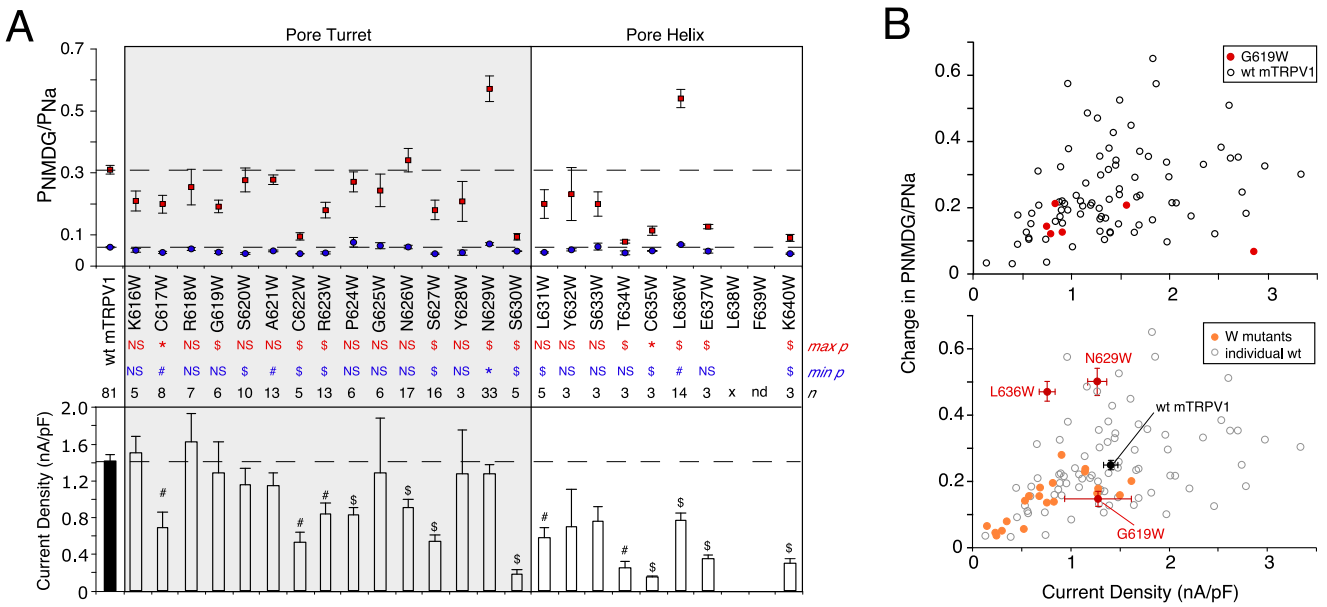

FIGURE 4. **Ionic selectivity changes following tryptophan scanning mutagenesis within the outer pore region of TRPV1.** *A,* summary of tryptophan scanning mutagenesis in mouse TRPV1. *Top,* minimum (*blue symbols*) and maximum (*red symbols*) P_{NMDG}/P_{Na} evoked by 1 μM RTX. *Bottom,* peak sodium current density measured at +20 mV. *Dashed lines* indicate wild type values. Data are presented as mean ± S.E. *, $p < 0.05$; #, $p < 0.01$; $, $p < 0.001$; *NS,* not statistically significant (mutant *versus* wild type, unpaired Student's *t* test). Regions of the pore, as annotated *above* the panel, are delineated by *shading*. *nd,* not determined; *x,* E_{rev} not measurable. *B,* change in P_{NMDG}/P_{Na} plotted as a function of peak sodium current density for wild type and mutant TRPV1. *Top,* individual recordings from cells expressing wild type mouse TRPV1 (*open symbols*) or mTRPV1-G619W (*red symbols*). *Bottom,* tryptophan mutant population. *Open symbols* represent individual wild type recordings. *Colored symbols* represent population means for wild type (*black*) and mutant (*orange*) channels. Mutants displaying a selective gain- or loss-of-function are shown in *red*. *Error bars* represent S.E. Wild type data are reproduced from Fig. 1.

corresponding position in mouse TRPV1. As observed previously for rat M644A, the mTRPV1-M645A substitution resulted in a clear gain-of-function. RTX-evoked $\Delta P_{NMDG}/P_{Na}$ was 0.44 ± 0.07 in M645A ($n = 8$), compared with 0.25 ± 0.01 in WT mTRPV1 ($p < 0.001$), a difference that stemmed from an increase in maximum NMDG permeability, and was accompanied by a small but significant increase in sodium current density (Fig. 5, *A* and *C*; Table 1). In contrast to the alanine substitution, replacing Met-645 with large residues uniformly reduced minimum P_{NMDG}/P_{Na}. In several cases (Lys, Trp, Tyr, Arg, and Leu), this reduction was associated with concomitant reductions in both maximal P_{NMDG}/P_{Na} and $\Delta P_{NMDG}/P_{Na}$ (Fig. 5, *A* and *C*). However, these permeability defects were also accompanied by a significant loss of sodium current density. These results may indicate that channel gating as a whole was compromised in these mutants, that the pore was constricted to a point where even sodium flux was impeded, or both. One mutant exhibiting a distinct phenotype was M645I. Neither sodium current density nor $\Delta P_{NMDG}/P_{Na}$ was statistically distinguishable from wild type; however, minimum P_{NMDG}/P_{Na} was significantly lower (0.04 ± 0.004 in M645I ($n = 9$) *versus* 0.06 ± 0.002 in WT mTRPV1 ($p < 0.01$)). Maximum P_{NMDG}/P_{Na} exhibited a trend toward a reduced value (0.24 ± 0.03 in M645I *versus* 0.31 ± 0.01 in WT mTRPV1) that did not reach

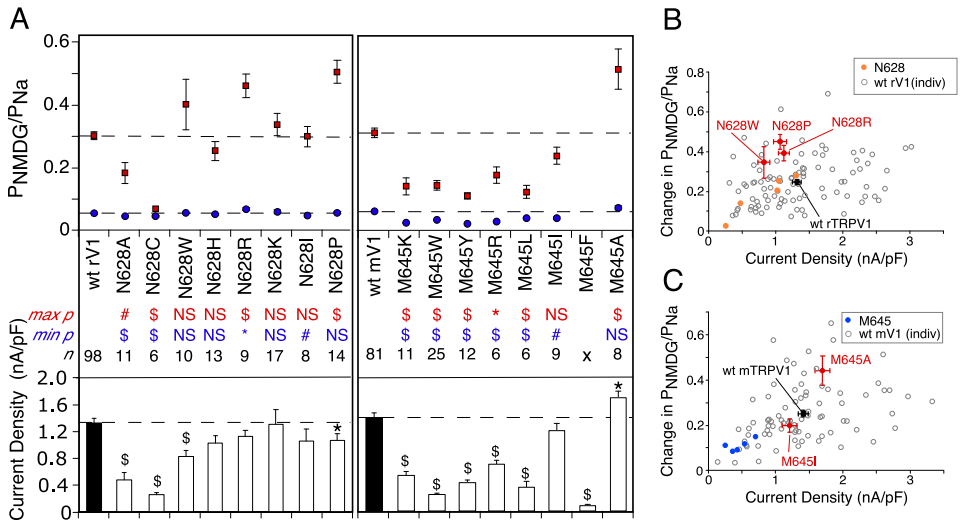

FIGURE 5. **Further mutagenesis at rTRPV1-N628 and mTRPV1-M645.** *A,* effects of substitution of rTRPV1-N628 (*left*) and mTRPV1-M645 (*right*) to various amino acid residues on NMDG permeability. *Top,* minimum (*blue symbols*) and maximum (*red symbols*) P_{NMDG}/P_{Na} evoked by 1 μM RTX. *Bottom,* peak sodium current density measured at +20 mV. *Dashed lines* indicate wild type values. Data are presented as mean ± S.E. *, $p < 0.05$; #, $p < 0.01$; $, $p < 0.001$; *NS,* not statistically significant (mutant *versus* wild type, unpaired Student's *t* test). *x,* E_{rev} not measurable. *B* and *C,* change in P_{NMDG}/P_{Na} plotted as a function of peak sodium current density for rTRPV1-N628 mutants (*B*) and mTRPV1-M645 mutants (*C*). *Open symbols* represent individual wild type recordings. *Filled symbols* represent population means for wild type (*black*) and mutant (Asn-628: *orange*; Met-645: *blue*) channels. Mutants displaying a selective gain- or loss-of-function are shown in *red*. *Error bars* represent S.E. Wild type data are reproduced from Fig. 1.

statistical significance (Fig. 5, *A* and *C*; Table 1). Based on its reduced minimal NMDG permeability, in the face of normal sodium current density, M645I was classified as a loss-of-function mutant. As with the rTRPV1-N628 residue, the choice of substituting amino acid at position Met-645 had a clear impact on NMDG permeability, and this was most evident when plotting $\Delta P_{NMDG}/P_{Na}$ against sodium current density (Fig. 5, *B* and *C*).

Because we had introduced substitutions on both the rat and mouse TRPV1 backgrounds during our screens, we sought to determine whether the mutant phenotypes were conserved across the two species. Indeed, this generally proved to be the case (Fig. 6, *A* and *B*; Table 1). The gains-of-function documented in the rat mutants N628P, F638A, and M644A were faithfully reproduced in the equivalent mouse channels. As described above, the gain-of-function recorded in mTRPV1-N629W was not statistically recapitulated in rTRPV1-N628W, but this latter mutant still showed a trend toward a greater $\Delta P_{NMDG}/P_{Na}$. The modest loss-of-function phenotype exhibited by mTRPV1-G619W was also recapitulated in rTRPV1-G618W. Furthermore, although mTRPV1-M645I was most noteworthy for a reduction in minimal P_{NMDG}/P_{Na} and exhibited only a trend toward reduced $\Delta P_{NMDG}/P_{Na}$, rTRPV1-M644I exhibited significantly reduced minimum, maximum, and $\Delta P_{NMDG}/P_{Na}$ (Fig. 6, *A* and *B*; Table 1). Because most phenotypes were more robust in rat mutants, all further characterization was performed in mutants of that species. As shown in Fig. 6*C*, although two of our mutants of interest (M644I and M644A) exhibited slight alterations in minimum P_{NMDG}/P_{Na}, the abnormal $\Delta P_{NMDG}/P_{Na}$ phenotypes in all mutants were attributable predominantly to increases or decreases in maximal P_{NMDG}/P_{Na} (mutant *versus* wild type TRPV1, Kaplan-Meier test).

As described above, measurement of peak outward sodium current density at +20 mV provided us with one means of accounting for any global changes in channel function in our mutants of interest. However, differences in the rate and extent of the E_{rev} change might have skewed the amplitude of the peak sodium current assayed at a fixed membrane potential. As an alternative means of evaluating general channel activation, we therefore analyzed maximum sodium conductance in our selected rTRPV1 mutants (see "Experimental Procedures"). For this approach, conductance was measured near E_{rev} to minimize the impact of voltage-dependent TRPV1 gating, which is most prominent at strongly positive potentials. As with sodium current density, alterations in $\Delta P_{NMDG}/P_{Na}$ among our mutants of interest were well out of proportion to any differences in maximal slope conductance (Fig. 6*D*), arguing strongly that the phenotypes we observed were not simply a reflection of alterations in general channel activity.

The kinetics with which the various rat TRPV1 mutants underwent agonist-evoked changes in E_{rev}, and consequently P_{NMDG}/P_{Na}, were not uniform. For example, while in WT rTRPV1, E_{rev} was found to shift with a time constant of 10.5 ± 0.6 s, and two gain-of-function mutants, N628W and M644A, recorded a significantly faster rate of change ($p < 0.001$) (Fig. 6, *E* and *F*). By contrast, the rate of E_{rev} increase was slower in two other gain-of-function mutants, N628P ($p < 0.01$) and F638A ($p < 0.001$), whereas the two mutants with a loss-of-function phenotype, G618W and M644I, did not deviate from wild type. The various mutants also differed with respect to sodium current kinetics. In WT rTRPV1, sodium current rise time was 3.5 ± 0.1 s. Although the N628W mutant did not differ from wild type, the N628P ($p < 0.05$), F638A ($p < 0.001$), M644A ($p < 0.01$), G618W ($p < 0.05$), and M644I ($p < 0.001$) mutants all displayed slower kinetics (Fig. 6*F*). The time constant of sodium current decay (3.4 ± 0.5 s in WT rTRPV1) was accelerated in the N628W ($p < 0.01$) and M644A ($p < 0.001$) mutants, slowed in the F638A mutant ($p < 0.01$), and unchanged in the remaining mutants under focus (Fig. 6*F*).

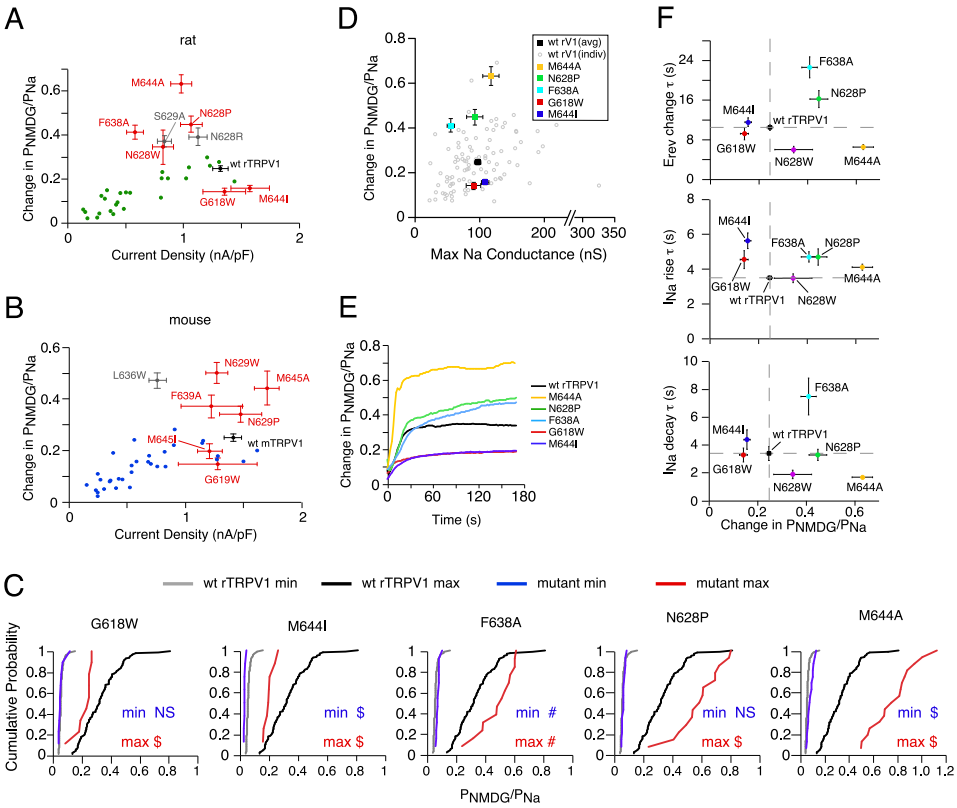

FIGURE 6. *A* and *B*, conservation of gain- and loss-of-function phenotypes across species. Change in P_{NMDG}/P_{Na} plotted as a function of peak sodium current density in rat (*A*) and mouse (*B*) TRPV1. *Colored symbols* represent population means for wild type (*black*) and mutant channels. Mutants showing a conserved phenotype between rat and mouse are labeled in *red*, and mutants demonstrating altered $\Delta P_{NMDG}/P_{Na}$ but examined in only one species are labeled in *gray*. All other mutants analyzed are represented by *green* (rat) or *blue* (mouse) symbols. *Error bars* represent S.E. Data for wild type and previously described mutant channels are reproduced from Figs. 1–5. *C*, cumulative distribution of minimum and maximum P_{NMDG}/P_{Na} during stimulation with 1 μM RTX among individual cells expressing wild type or mutant rat TRPV1. #, $p < 0.01$; $, $p < 0.001$; *NS*, not statistically significant (Kaplan-Meier test). Data are taken from the same experiments as Fig. 5*A*. *D*, RTX evoked change in P_{NMDG}/P_{Na} plotted as a function of peak sodium slope conductance. *Open symbols* represent individual wild type recordings. *Colored symbols* represent population means for wild type and mutant rat TRPV1. *Error bars* represent S.E. *E*, representative traces showing time-dependent changes in P_{NMDG}/P_{Na} during stimulation with 1 μM RTX in wild type and mutant rat TRPV1. *F*, time constants for rate of RTX-evoked change in E_{rev} (*top*), sodium current peak (*middle*), and sodium current decay (*bottom*) plotted as a function of change in P_{NMDG}/P_{Na} for wild type and mutant rat TRPV1. *Dashed lines* indicate wild type values. All data are presented as mean ± S.E.

However, as described above, sodium current decay in this setting is unlikely to reflect channel inactivation, because other factors can account for this decline and because sodium currents did not decay in symmetrical sodium solutions. Regardless, although mutations in the rat TRPV1 outer pore can perturb multiple kinetic parameters of channel function, none of these parameters are strictly predictive of the magnitude of RTX-induced change in P_{NMDG}/P_{Na}.

All data presented above were collected using a saturating concentration of RTX as the TRPV1 stimulus. To exclude any nonspecific effects of saturating agonist concentrations, NMDG permeability in wild type and mutant channels was reassessed in the presence of 10 nM RTX. Under these conditions, the gain- and loss-of-function phenotypes characterized at 1 μM RTX were preserved. $\Delta P_{NMDG}/P_{Na}$ was 0.54 ± 0.03 in the M644A mutant ($n = 20$), significantly greater than the value of 0.29 ± 0.03 recorded in WT rTRPV1 ($p < 0.001$, $n = 22$). The RTX-evoked change in NMDG permeability trended toward greater values in the N628P channel (0.33 ± 0.04, $n = 15$), although the difference between this mutant and wild type did not reach statistical significance. Meanwhile, both the G618W and M644I channels showed reduced $\Delta P_{NMDG}/P_{Na}$ of 0.19 ± 0.02 ($p < 0.01$ *versus* WT rTRPV1, $n = 9$) and 0.21 ± 0.02 ($p < 0.05$, $n = 9$), respectively.

To independently verify the phenotypes observed in our patch clamp experiments, we examined agonist-evoked uptake of the large cationic dye, YO-PRO1, in selected gain-of-function (N628P and M644A) and loss-of-function (G618W and M644I) rTRPV1 mutants. Exposure of TRPV1- or control vector-transfected HEK293 cells to YO-PRO1 in the absence of agonist resulted in a transient increase in cellular fluorescence whose rate subsided after ~1 min (Fig. 7*A*). Addition of RTX (1 μM) produced a slow onset increase in YO-PRO1 uptake rate in cells expressing WT rTRPV1, but not in vector control cells, that reached a plateau within ~60 s (Fig. 7*A*). Consistent with the results of our NMDG permeability experiments, cells expressing either N628P or M644A exhibited a significantly greater rate of RTX-evoked YO-PRO1 uptake (Fig. 7, *A* and *B*), whereas cells expressing G618W or M644I exhibited an uptake rate significantly lower than wild type (Fig. 7, *C* and *D*). To exclude the possibility that these YO-PRO1 uptake differences were attributable to differential expression levels of the various mutants, we immunoblotted lysates from TRPV1-transfected HEK293 cells with antibodies recognizing a C-terminal epitope

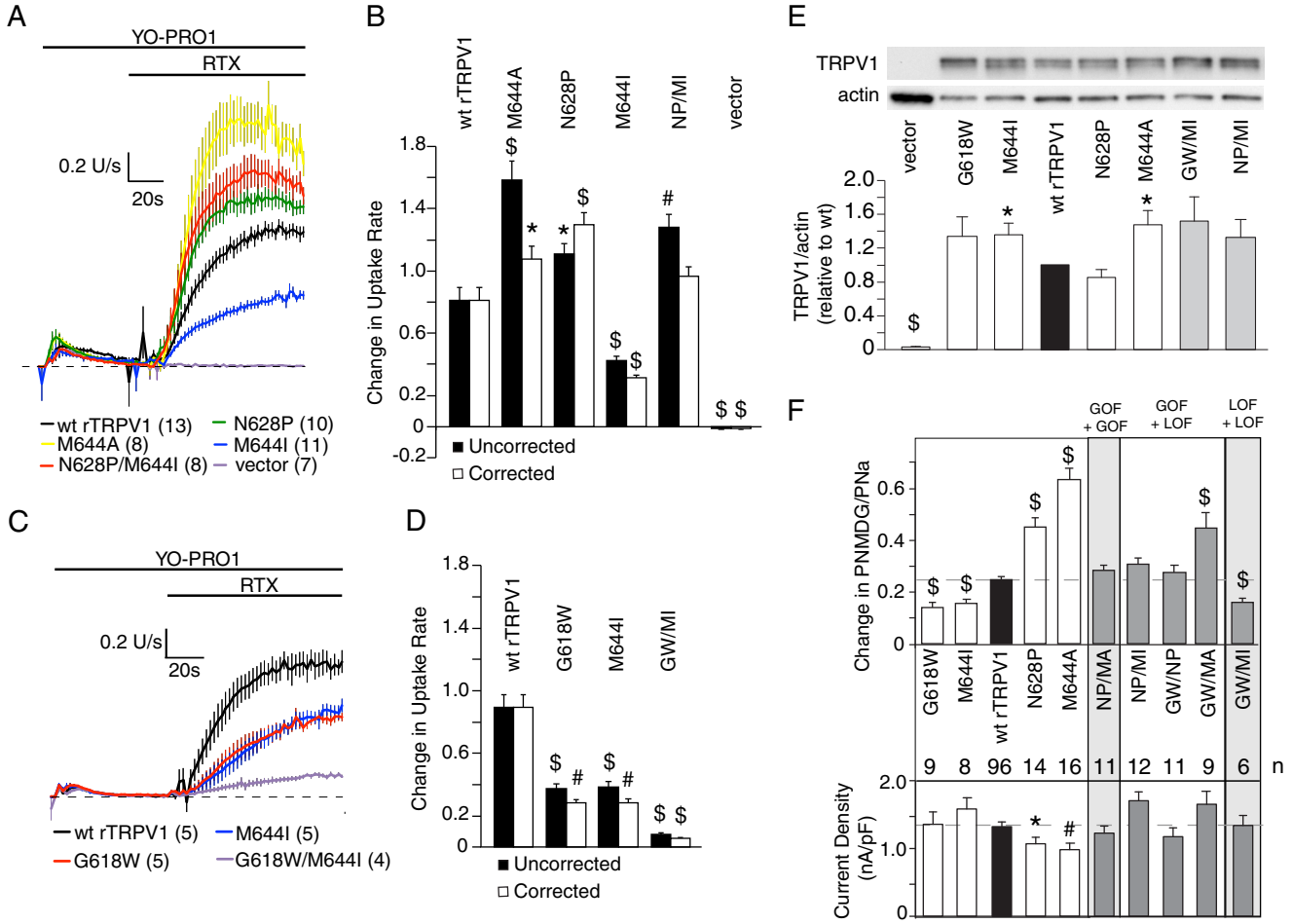

FIGURE 7. **RTX-evoked YO-PRO1 uptake via TRPV1 pore mutants.** *A* and *C*, rate of YO-PRO1 uptake via wild type or mutant rat TRPV1, during stimulation with 1 μM RTX. Data were normalized to the average maximum dye uptake rate recorded from wild type coverslips on the same day, and they are presented as mean ± S.E. averaged across the number of coverslips indicated in *parentheses*. *B* and *D*, change in rate of YO-PRO1 uptake from baseline, measured just prior to RTX addition, to the period 60–80 s after RTX addition, without (*black bars*) and with (*white bars*) correction for channel protein expression. Data were normalized to the maximum change in dye uptake rate recorded from wild type coverslips on the same day, and they are presented as mean ± S.E. *, $p < 0.05$; #, $p < 0.01$; $, $p < 0.001$ (mutant *versus* wild type, unpaired Student's *t* test). Residue numbers have been omitted from double mutant names for clarity (*NP*, N628P; *MI*, M644I; *GW*, G618W). *E*, immunoblot analysis of TRPV1 and actin expression in transfected HEK293 cells. Mutant channel expression was normalized to expression of wild type TRPV1 (*black bar*) from concurrent transfections. Channels containing a single mutation are represented by *white bars*; double mutants are represented by *gray bars*. Data are presented as mean ± S.E. Wild type, $n = 6$ independent transfections; mutants and vector, $n = 4$. No S.E. is presented for wild type. *F, top*, RTX-evoked change in P_{NMDG}/P_{Na} in wild type and mutant rat TRPV1. *Bottom*, peak sodium current density measured at +20 mV. Wild type TRPV1 is represented by a *black bar*; channels containing a single mutation are represented by *white bars*; double mutants are represented by *gray bars*. *GOF*, gain-of-function; *LOF*, loss-of-function; *MA*, M644A. Data are presented as mean ± S.E. *, $p < 0.05$; #, $p < 0.01$; $, $p < 0.001$ (mutant *versus* wild type, unpaired Student's *t* test). Wild type and single mutant NMDG permeability data are reproduced from Figs. 1–5. *Dashed lines* indicate wild type levels.

far from the mutated region. We observed some variability in expression levels of the mutant channel proteins in pooled transfected cell populations (Fig. 7*E*). However, following correction of the agonist-evoked changes in YO-PRO1 uptake rate for these values, the overall phenotypes of both gain- and loss-of-function mutants were preserved (Fig. 7, *B* and *D*). Together, these findings verify that the phenotypes observed in this group of mutants are not an artifact of the electrophysiology method.

Interactions among Residues Affecting Dynamic Ionic Selectivity—Mutations giving rise to alterations in dynamic ionic selectivity in TRPV1 were located in three distinct areas of the pore as follows: the pore turret (rat G618W, N628P, and S629A; mouse G619W and N629P), the pore helix (rat F638A; mouse L636W and F639A), and the selectivity filter (rat M644A and M644I; mouse M645A and M645I). We paired some of these mutations within the same channel cDNA to determine whether they would interact positively or negatively, with respect to ionic selectivity. Pairing two gain-of-function mutations (M644A and N628P) produced a channel that resembled wild type in terms of its ability to permeate NMDG ions ($n = 11$) (Fig. 7*F*). Thus, the gains-of-function conferred by mutations in these two areas of the pore are apparently not additive. The double G618W/M644I mutant, which combined two loss-of-function mutations, exhibited an RTX-evoked $\Delta P_{NMDG}/P_{Na}$ lower than that of WT rTRPV1, but this decrease was not distinguishable from that recorded in either of the two single mutants ($n = 6$) (Fig. 7*F*). However, when we evaluated the G618W/M644I channel in the YO-PRO1 uptake assay, the rate of RTX-evoked dye uptake was significantly lower via this double mutant compared with either the G618W or M644I single mutants ($p < 0.001$), regardless of whether the rate was corrected for channel protein expression (Fig. 7, *C–E*). The apparent discrepancy between the two assays might be due to the difference in size between NMDG (196 Da) and YO-PRO1 (630

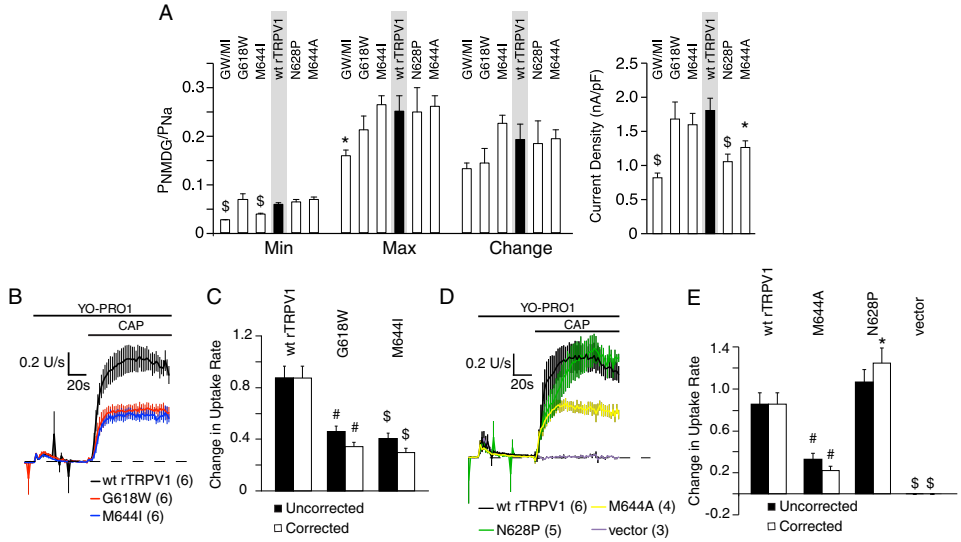

FIGURE 8. **Capsaicin-evoked large cation uptake via TRPV1 pore mutants.** *A, left,* values for minimum, maximum, and change in P_{NMDG}/P_{Na} evoked by 10 μM capsaicin in wild type and mutant rat TRPV1. *Right,* peak sodium current density measured at +20 mV. Data are presented as mean ± S.E. *, $p < 0.05$; #, $p < 0.01$; $, $p < 0.001$ (mutant *versus* wild type, unpaired Student's *t* test). G618W/M644I, $n = 17$; G618W, $n = 6$; M644I, $n = 7$; wild type, $n = 20$; N628P, $n = 12$; M644A, $n = 14$. *B* and *D,* rate of YO-PRO1 uptake via wild type or mutant rat TRPV1, during stimulation with 10 μM capsaicin. Data were normalized to the average maximum dye uptake rate recorded from wild type coverslips on the same day and are presented as mean ± S.E. averaged across the number of coverslips indicated in *parentheses*. *C* and *E,* change in rate of YO-PRO1 uptake from baseline, measured just prior to capsaicin addition, to the period 60–80 s after capsaicin addition, without (*black bars*) and with (*white bars*) correction for channel protein expression (from Fig. 7*E*). Data were normalized to the maximum change in dye uptake rate recorded from wild type coverslips on the same day and are presented as mean ± S.E. *, $p < 0.05$; #, $p < 0.01$; $, $p < 0.001$ (mutant *versus* wild type, unpaired Student's *t* test).

Da) if, for example, deficits in permeability to the larger cation were easier to observe. If so, this would suggest that combination of the G618W and M644I mutations does indeed result in additive functional constriction of the TRPV1 pore.

We also examined the consequences of pairing gain-of-function with loss-of-function mutations. Assessment of RTX-evoked changes in NMDG permeability in three such double mutants (G618W/N628P, $n = 11$; G618W/M644A, $n = 9$; and N628P/M644I, $n = 12$) revealed that the opposing phenotypes of the single mutations combined to produce an intermediate phenotype that closely resembled the wild type channel (Fig. 7*F*). We examined one of these double mutants (N628P/M644I) in the dye uptake assay. RTX-evoked YO-PRO1 uptake was either greater than wild type (assessed without correction for TRPV1 expression level) or similar to wild type (corrected for expression level) in this mutant, and in either case was significantly greater than that in the M644I single mutant (Fig. 7, *A, B,* and *E*). Thus, in both assays, the N628P mutation in the pore turret domain appears to compensate at least partially for the large cation permeability defect in M644I, even though the latter is located directly within the selectivity filter.

Some Mutations Affect Dynamic Ionic Selectivity in an Agonist-specific Manner—We previously reported that diverse agonists alter TRPV1 P_{NMDG}/P_{Na} at different rates and/or to varying extents and that capsaicin and RTX, in particular, exhibit both kinetic and qualitative differences in their abilities to evoke these changes (10). Capsaicin and RTX have been shown to produce kinetically distinct patterns of TRPV1 gating at the single channel level (27). Furthermore, in a recent study, both the selectivity filter and the lower pore gate of capsaicin-bound TRPV1 were shown to differ structurally from those of a TRPV1 molecule bound simultaneously to RTX and a double-knot spider toxin specific for TRPV1 (DkTx) (4). We therefore evaluated dynamic NMDG permeability induced by capsaicin (10 μM) in several of the mutants identified in this study. Surprisingly, the capsaicin-evoked $\Delta P_{NMDG}/P_{Na}$ was statistically indistinguishable between WT rTRPV1 (0.19 ± 0.04, $n = 16$) and any of four mutant channels analyzed as follows: N628P (0.18 ± 0.05, $n = 12$); M644A (0.19 ± 0.02, $n = 14$); G618W (0.14 ± 0.03, $n = 6$); and M644I (0.23 ± 0.02, $n = 7$) (Fig. 8*A*). Peak sodium current density was significantly lower than wild type in the N628P and M644A mutants. Nevertheless, on the basis of data collected using RTX as the agonist, the currents produced were still within the range where we would expect an ionic selectivity phenotype to be detectable. Minimum P_{NMDG}/P_{Na} was reduced in the M644I channel compared with wild type (0.04 ± 0.001 in M644I *versus* 0.06 ± 0.003 in WT rTRPV1 ($p < 0.001$)), supporting the earlier conclusion that the introduction of the isoleucine residue leads to a constriction of the channel pore. However, maximum NMDG permeability reached the same level as recorded in wild type rat TRPV1 (0.26 ± 0.017 in M644I *versus* 0.25 ± 0.032 in WT rTRPV1) (Fig. 8*A*). In the G618W/M644I double mutant, both minimum and maximum P_{NMDG}/P_{Na} were reduced (minimum P_{NMDG}/P_{Na}, 0.03 ± 0.001 ($p < 0.001$ *versus* WT rTRPV1); maximum P_{NMDG}/P_{Na}, 0.16 ± 0.012 ($p < 0.05$, $n = 17$)), although the overall increase in NMDG permeability remained statistically indistinguishable from WT rTRPV1 ($\Delta P_{NMDG}/P_{Na}$, 0.13 ± 0.012 in G618W/M644I *versus* 0.19 ± 0.04 in WT rTRPV1) (Fig. 8*A*). Even the trend toward a reduced $\Delta P_{NMDG}/P_{Na}$ in the double mutant was observed in the context of a significantly reduced sodium current density, and therefore it could not be interpreted as a selective loss-of-function.

We next examined YO-PRO1 uptake in the four single mutants. In contrast to the NMDG permeability findings, the rates of capsaicin-evoked dye uptake were reduced in the

G618W and M644I channels (Fig. 8, *B* and *C*), consistent with our observations using RTX as the agonist. In the N628P mutant, capsaicin-evoked YO-PRO1 uptake was similar to (when assessed without correction for protein expression) or slightly higher than (with correction) that observed in WT rTRPV1 (Fig. 8, *D* and *E*). Unexpectedly, however, M644A, which had exhibited a clear gain-of-function phenotype when stimulated with RTX, paradoxically exhibited a significantly reduced rate of capsaicin-evoked YO-PRO1 uptake, whether corrected for protein expression or not (Fig. 8, *D* and *E*). Together, these data demonstrate that some but not all phenotypic consequences of TRPV1 pore mutagenesis were conserved between vanilloid agonists and further suggest that the sensitivity with which these phenotypes can be resolved differs between the electrophysiological and dye uptake assays.

Examination of Additional Pore Domain Mutants—In a recent high throughput mutagenesis screen of rat TRPV1, the N628K substitution as well as two substitutions in the small pore turret region that connects the selectivity filter with TM6, N652T, and Y653T, were each shown to compromise channel activation by heat (21). A triple N628K/N652T/Y653T mutant was shown to be even more defective in heat responsiveness than any single mutant, and this defect was attributed to impaired stabilization of a long lifetime single channel open state. Although the N628K mutant did not exhibit an abnormal NMDG permeability phenotype in our hands (Fig. 5, *A* and *B*), the gain-of-function ionic selectivity phenotype we observed following other substitutions at this residue prompted us to explore whether the N652T or Y653T channels might exhibit alterations in RTX-evoked dynamic NMDG permeability. The N652T mutant exhibited a trend toward increased NMDG permeability change that did not reach statistical significance ($\Delta P_{NMDG}/P_{Na}$, 0.31 ± 0.04 in N652T ($n = 13$) *versus* 0.25 ± 0.01 in WT rTRPV1) (Fig. 9, *A* and *B*). The Y653T mutant did differ from WT rTRPV1, but in contrast to several of our mutations at Asn-628, it showed a modestly reduced ability to permeate NMDG ($\Delta P_{NMDG}/P_{Na}$, 0.19 ± 0.02 in Y653T ($p < 0.05$ *versus* WT rTRPV1, $n = 10$)) (Fig. 9, *A* and *B*). Based on these findings, reduced heat sensitivity and enhanced dynamic NMDG permeability in TRPV1 appear to be dissociable phenotypes.

We next evaluated the effects on ion selectivity dynamics of mutagenesis at rTRPV1-N604, a residue within the large pore turret domain that is the sole site of TRPV1 *N*-linked glycosylation. It was recently reported that preventing glycosylation by mutating this amino acid to threonine could ablate capsaicin-induced uptake of YO-PRO1 (28). We re-examined large cation permeability in this mutant using both electrophysiology and YO-PRO1 imaging. Stimulation of rTRPV1-N604T with 1 μM RTX increased P_{NMDG}/P_{Na} to the same extent as observed in the wild type channel ($\Delta P_{NMDG}/P_{Na}$, 0.2 ± 0.03 in N604T ($n = 8$) *versus* 0.25 ± 0.01 in WT rTRPV1) (Fig. 9, *A* and *B*). The rate of RTX-evoked YO-PRO1 uptake via N604T was reduced relative to wild type (Fig. 9, *C* and *D*); however, the magnitude of this reduction was only one-third approximately, even when uptake was corrected for protein expression levels. Successful inhibition of *N*-linked glycosylation in this mutant was supported by immunoblot analysis, which demonstrated that the normal TRPV1 doublet had collapsed into a single more mobile species (Fig. 9*E*). As seen with RTX, capsaicin (1 μM) stimulation of N604T increased P_{NMDG}/P_{Na} to the same extent as observed in WT rTRPV1 (Fig. 9*F*). Also similar to our RTX findings, we observed a slight reduction in capsaicin-evoked YO-PRO1 uptake via this mutant (Fig. 9, *G* and *H*). Still, the remaining uptake response was substantial. Together, these data lead us to conclude that glycosylation of TRPV1 Asn-604 is not essential for dynamic ionic selectivity, but it may influence its amplitude, especially when assessed by YO-PRO1 uptake.

The final residue we mutated was mTRPV1-E637, which is situated within the pore helix, and has been speculated to form a salt bridge with Lys-640 (29). To address the potential importance of this interaction to large cation permeability, we replaced Glu-637 with a number of chemically distinct amino acids. Three of these mutants (Pro, Arg, and Lys) were nonfunctional in the presence of RTX, and a further three mutants (His, Asn, and Tyr) displayed normal NMDG permeability dynamics compared with wild type. The remaining five mutant channels (Ala, Gln, Thr, Asp, and Trp) showed decreased $\Delta P_{NMDG}/P_{Na}$, but in the context of a significantly reduced sodium current, and none deviated significantly from the wild type current *versus* $\Delta P_{NMDG}/P_{Na}$ relationship (Fig. 9*I*). Thus, this residue appears not to be essential for dynamic ionic selectivity.

Structural Modeling of TRPV1 Dynamic Ionic Selectivity Mutants—The TRPV1 atomic structure was recently determined in three different activation states as follows: in the apo-form; bound to capsaicin; and simultaneously bound to both RTX and the tarantula-derived DkTx (3, 4). Among the major findings of those studies was that the selectivity filter domain was constricted in the absence of exogenous agonist, with recorded pore diameters of 4.6 Å at the level of Gly-643 and 5.9 Å at the neighboring Met-644 residue, but it expanded with RTX/DkTx stimulation to produce diameters of 7.6 and 13.0 Å at Gly-643 and Met-644, respectively. Opening of the selectivity filter is accompanied by a tilting of the pore helix away from the central pore axis. Expansion of the lower channel pore at TM6 residue Ile-679 was also observed in both capsaicin- and RTX/DkTx-bound structures, but the absence of significant changes in the selectivity filter and pore helix domains in the capsaicin-bound channel led the authors to conclude that this latter structure represents a partially activated channel state. Furthermore, although the RTX/DkTx-bound structure showed that changes in the upper TRPV1 pore occur during gating, the pore diameter in this activated state remains too small to accommodate large cations such as YO-PRO1. We nevertheless utilized this collection of structures to model several of our ion selectivity mutants, operating under the assumption that the RTX/DkTx-bound structure represents a conformational intermediate on the way toward full selectivity filter expansion and that changes in the ability of TRPV1 to adopt this state would therefore influence subsequent increases in large cation permeability. The positions of these mutations within the RTX/DkTx-bound structure are summarized in Fig. 10*A*.

We began by examining the location of two pore helix residues identified in our study to be important for ionic selectivity,

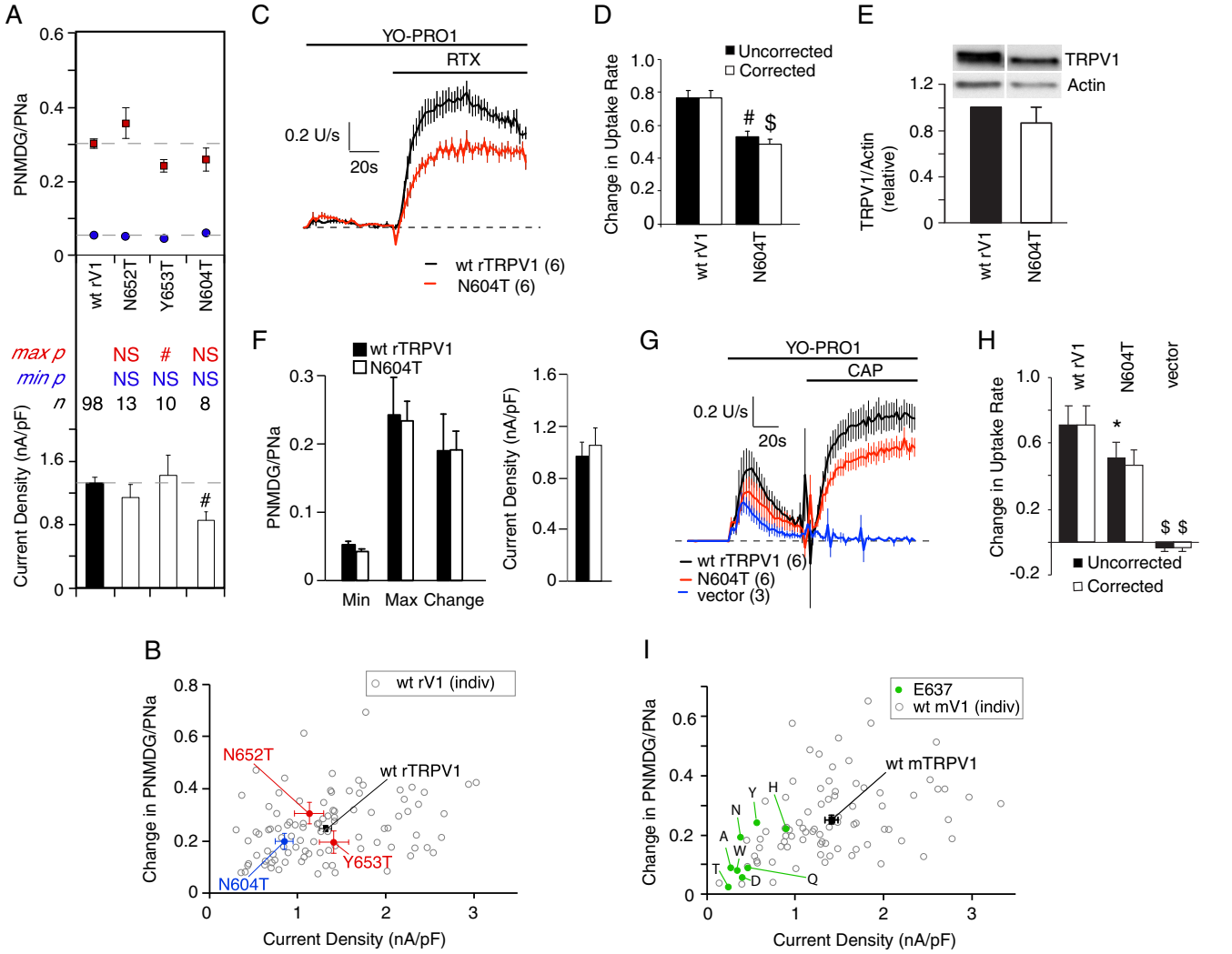

FIGURE 9. **RTX-evoked large cation permeability in heat-insensitive or glycosylation-deficient rat TRPV1 mutants.** *A, top,* minimum (*blue symbols*) and maximum (*red symbols*) P_{NMDG}/P_{Na} evoked by 1 μM RTX. *Bottom,* peak sodium current density measured at +20 mV. *Dashed lines* indicate wild type values. Data are presented as mean ± S.E. *, $p < 0.05$; #, $p < 0.01$; $, $p < 0.001$; *NS,* not statistically significant (mutant *versus* wild type, unpaired Student's *t* test). *B,* change in P_{NMDG}/P_{Na} plotted as a function of peak sodium current density for wild type and mutant TRPV1. *Open symbols* represent individual wild type recordings. *Colored symbols* represent population means for wild type (*black*), heat-insensitive (*red*), and glycosylation-deficient (*blue*) TRPV1 channels. *Error bars* represent S.E. Wild type data are reproduced from Fig. 1. *C,* rate of YO-PRO1 uptake via wild type or rTRPV1-N604T channels, during stimulation with 1 μM RTX. Data were normalized to the average maximum dye uptake rate recorded from wild type coverslips on the same day and are presented as mean ± S.E. averaged across the number of coverslips indicated in *parentheses*. *D,* change in rate of YO-PRO1 uptake from baseline, measured just prior to RTX addition, to the period 60–80 s after RTX addition, without (*black bars*) and with (*white bars*) correction for channel protein expression. Data were normalized to the maximum change in dye uptake rate recorded from wild type coverslips on the same day and are presented as mean ± S.E. *, $p < 0.05$; #, $p < 0.01$; $, $p < 0.001$ (mutant *versus* wild type, unpaired Student's *t* test). *E,* immunoblot analysis of TRPV1 and actin expression in transfected HEK293 cells. Mutant N604T channel expression was normalized to expression of wild type TRPV1 from concurrent transfections. Data are presented as mean ± S.E. from three independent transfections per group. No S.E. is presented for wild type. *F, left,* values for minimum, maximum, and change in P_{NMDG}/P_{Na} evoked by 1 μM capsaicin in wild type and rTRPV1-N604T channels. *Right,* peak sodium current density measured at +20 mV. Data are presented as mean ± S.E. Wild type, $n = 11$; N604T, $n = 8$. *G,* rate of YO-PRO1 uptake via wild type or rTRPV1-N604T channels, during stimulation with 1 μM capsaicin. Data were normalized to the average maximum dye uptake rate recorded from wild type coverslips on the same day and are presented as mean ± S.E. averaged across the number of coverslips indicated in *parentheses*. *H,* change in rate of YO-PRO1 uptake from baseline, measured just prior to capsaicin addition, to the period 60–80 s after capsaicin addition, without (*black bars*) and with (*white bars*) correction for channel protein expression. Data were normalized to the maximum change in dye uptake rate recorded from wild type coverslips on the same day and are presented as mean ± S.E. *, $p < 0.05$; #, $p < 0.01$; $, $p < 0.001$ (mutant *versus* wild type, unpaired Student's *t* test). *I,* change in P_{NMDG}/P_{Na} plotted as a function of peak sodium current density for wild type and mTRPV1-E637 mutant populations. *Open symbols* represent individual wild type recordings. *Colored symbols* represent population means for wild type (*black*) and mutant (*green*) channels. Specific amino acid substitutions are indicated. *Error bars* represent S.E. Wild type NMDG permeability data are reproduced from Fig. 1.

namely mouse Leu-636 (equivalent to rat Leu-635) and rat Phe-638. Leu-635 is conserved among TRPV1-TRPV4, whereas Phe-638 is conserved among all TRPV family members. Strikingly, these residues are located on the same face of the pore helix, one turn apart, and are oriented away from the pore axis (Fig. 10*A*). Examination of the potential interactions of these residues revealed that, although they do not obviously contact other residues on the same channel subunit, they are closely juxtaposed to one face of TM6 on the adjacent subunit. Furthermore, comparison of apo- and RTX/DkTx-bound TRPV1 structures (Fig. 10, *B* and *C*) showed that, during activation, the tilt of the pore helix promotes tighter packing between these two residues and the TM6 residues Ile-660, Leu-664, and Ile-668, suggesting that

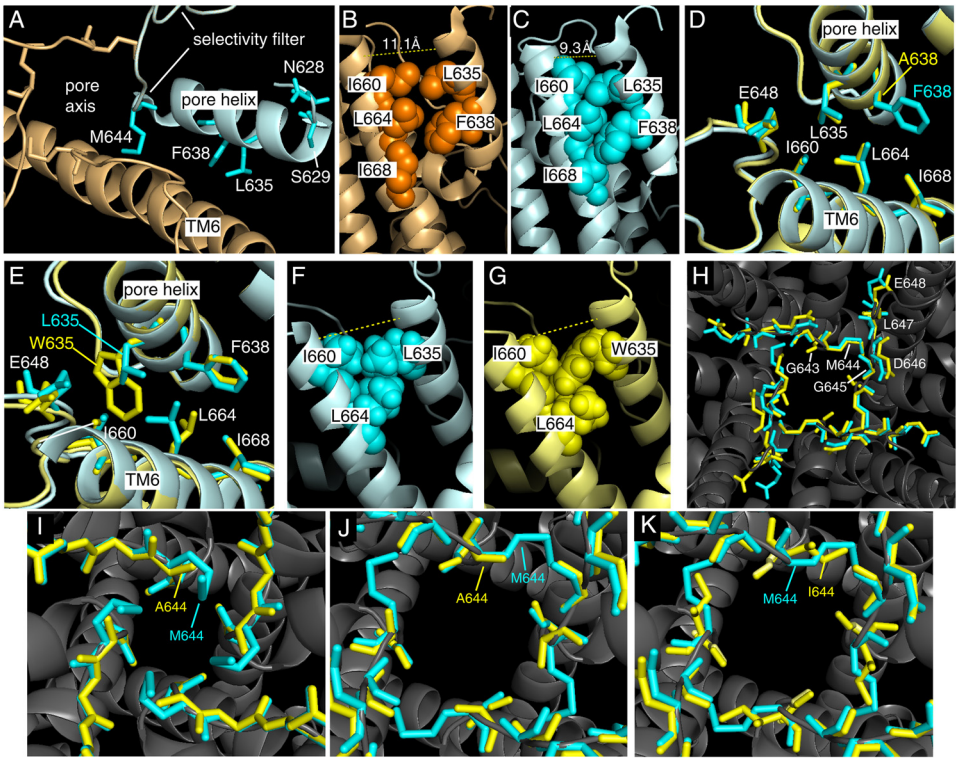

FIGURE 10. **Structural modeling of TRPV1 ion selectivity mutants.** *A,* locations of several key loci within the wild type TRPV1 pore helix and selectivity filter where specific substitutions produce gain- or loss-of-function of large cation permeability. For clarity, only residues on a given subunit (*cyan*) are shown. The TM6 helix of one adjacent subunit and the Met-644 side chains of all three other subunits are illustrated in *brown*. *B* and *C,* agonist-evoked changes in proximity of the pore helix to TM6 of the adjacent subunit. *Spheres* illustrate the proximity of wild type side chains of Leu-635 and Phe-638 residues in the pore helix to the indicated TM6 residues in the apo-TRPV1 structure (*B*) and in the RTX/DkTx-bound structure (*C*). *D* and *E,* comparison of side chain conformations at the pore helix-TM6 interface in the agonist-bound structure between wild type TRPV1 (*cyan*) and mutants F638A (*D*) and L635W (*E*). *F* and *G,* side chain interdigitation at the pore helix-TM6 interface in agonist-bound structures of wild type TRPV1 (*F, cyan*) and mutant L635W (*G, yellow*). *H,* comparison of selectivity filter side chain conformations in agonist-bound structures of wild type TRPV1 (*cyan*) and mutant L635W (*yellow*). *I* and *J,* selectivity filter side chain conformations in apo- (*I*) and agonist-bound (*J*) structures of wild type TRPV1 (*cyan*) and mutant M644A (*yellow*). *K,* selectivity filter side chain conformations in agonist-bound structures of wild type TRPV1 (*cyan*) and mutant M644I (*yellow*). Views in *A* and *H–K* are from the extracellular environment. Views in *B, C, F,* and *G* are from the plane of the membrane. Structures in *A–C* are from the published Protein Data Bank files (3, 4). Structures in the remaining panels have been energy-minimized. *H–K,* the *gray ribbon* structure shown is that of wild type TRPV1. Distances are in angstroms.

steric interactions with TM6 might promote and/or constrain movement of the pore helix.

To explore the possible structural mechanisms by which these and other amino acid substitutions highlighted in our functional assays produced gain- or loss-of-function, we performed energy minimization calculations on the TRPV1 models with and without each amino acid substitution. An energetic penalty was imposed on the movement of the Cα to prevent excessive departures of backbone structure from the original models of wild type TRPV1. Under these conditions, energy minimization of both the apo- and RTX/DkTx-bound wild type TRPV1 models yielded structures that were highly similar to the original structures and preserved two key features of channel activation, namely tilting of the pore helix toward TM6 of the adjacent subunit (data not shown) and expansion of the pore at the level of Met-644 (data not shown). This permitted us to proceed with modeling of the mutant channels.

As described above, the F638A substitution augmented minimal NMDG permeability and produced an even greater increase in maximal P_{NMDG}/P_{Na}. When this substitution was modeled on the RTX/DkTx-bound structure, there was no discernible impact on the side chains of residues in the selectivity filter (data not shown) or on the side chains of residues on TM6 that oppose the pore helix (Fig. 10*D*). However, elimination of the bulky phenyl ring at position 638 removed a substantial mass at the interface between these two helices. The resulting gap might permit a greater excursion of the lower pore helix, carrying the bottom of the selectivity filter away from the pore axis and thereby facilitating large cation permeation. Although no such movement was evident in our energy-minimized model, that might simply be due to the imposed backbone structural constraints.

A different picture emerged from modeling the rat mutant L635W, the equivalent of mouse L636W, another gain-of-function mutant. In this case, we identified two potential mechanisms for enhanced RTX-evoked NMDG permeability. First, in the RTX/DkTx-bound structure, the L635W mutation perturbed the side chain orientations of Ile-660 and Leu-664 (Fig. 10*E*) and resulted in more extensive side chain packing of the pore helix against TM6 (Fig. 10, *F* and *G*). This tighter packing, coupled with the fact that the entropic penalty for constraining the conformation of tryptophan in a helix is less than that for leucine, might stabilize the pore helix tilt and consequently the expanded pore conformation. Second, L635W substitution in the RTX/DkTx-bound structure resulted in conformational rearrangements of the side chains of two residues within the

selectivity filter, Glu-648 and Asp-646, asymmetrically across the four subunits (Fig. 10, *E* and *H*). Although the narrowest part of the pore at Met-644 showed little change at three of four subunits in this model, alterations in the two acidic residues might independently affect large cation flux through the pore. In contrast, the L635W mutation produced minimal structural effects on either the carbon backbone or side chain orientations in the apo-TRPV1 structure (data not shown), consistent with the differential effects of this mutation on minimal *versus* maximal NMDG permeability.

We next modeled the potential structural consequences of the phenotypic mutations at Met-644. The M644A substitution increased both minimal and maximal NMDG permeability, as well as YO-PRO1 uptake, in response to RTX. In the apo conformation, the Met-644 side chain juts directly into the pore axis. Substitution of alanine for methionine substantially reduced the bulk of this pore-impinging side chain, increasing the minimal distance between opposing residue 644 side chains from ~5.2 to 8.3 Å (Fig. 10*I*), providing one potential explanation for the increase in minimal P_{NMDG}/P_{Na} in this mutant. In the RTX/DkTx-bound state, the Met-644 side chain is not pointing toward the pore axis but rather lies circumferentially along the perimeter of the pore (Fig. 10*J*). Under these conditions, mutation to alanine had no impact on the diameter of the modeled pore (Fig. 10*J*). However, if the side chain of Met-644 restricts further pore expansion, this constraint might be alleviated by the introduction of the alanine residue. A mutually nonexclusive explanation is that the reduced bulk of the side chain of 644A might simply impose less of a barrier to TRPV1 transition from the constricted to the expanded pore conformation. The paradoxical inhibitory effect of alanine substitution on capsaicin-evoked YO-PRO1 uptake could be explained if we again consider the circumferential orientation of Met-644 and assume that capsaicin induces an expanded pore state that is similar but not identical to that evoked by RTX/DkTx. In this case, the M644A substitution might allow the perimeter to tighten like an iris in the presence of capsaicin, producing a narrower selectivity filter than achieved with RTX.

The M644I mutant reduced both minimal and maximal NMDG permeability, as well as YO-PRO1 uptake, in response to RTX. In the RTX/DkTx-bound M644I model structure, we observed no obvious change in selectivity filter architecture, beyond the mutated side chain (Fig. 10*K*). However, the new methyl group at the β-carbon position, which extends parallel to the pore axis and perpendicular to the plane of the wild type methionine side chains, might interfere with the approach of large cations to this narrow segment of the selectivity filter. In addition, because the isoleucine side chain typically exhibits fewer energetically permissible conformations than that of methionine, this substitution might impede the transition to the enlarged pore state, regardless of its impact on final pore conformation.

Finally, we examined phenotypic mutations in the pore turret domain. Rat TRPV1-G618 lies within a section of the pore turret (residues 604–626) that was omitted from the modified TRPV1 channel used for the structural studies, and therefore it could not be modeled. The Asn-628 and Ser-629 residues meanwhile are located just above the pore helix (Fig. 10*A*), in a region that moves substantially following the binding of RTX and DkTx, as a consequence of the tilting of the pore helix. Comparison of the apo- and RTX/DkTx-bound structures revealed no obvious changes in interactions with other residues on the same or adjacent subunits following channel activation (data not shown). However, the omission of residues 604–626 from the experimental structures prevented us from evaluating potential changes in interactions of Asn-628 and Ser-629 with nearby pore turret residues. Therefore, structural interpretation of the significance of dynamic ionic selectivity phenotypes in Gly-618, Asn-628, and Ser-629 mutants will need to await models that represent a more complete channel.

DISCUSSION

Through systematic mutagenesis of the TRPV1 outer pore, we have identified residues in the pore turret, pore helix, and selectivity filter domains that influence agonist-evoked dynamic permeability to large cations. In addition to providing insight into the biophysical basis of this dynamic process, the fact that large cation selectivity could be finely tuned by outer pore mutations bolsters the argument (10) that large cations pass through the TRPV1 pore itself, as opposed to permeating a separate channel protein. A recent study has unmasked an alternative ion permeation pathway in the TRPM3 channel, distinct from the central ion-conducting pore (30). Opening of this second pathway gives rise to an inwardly rectifying cationic current that is believed to be analogous to the "omega current," previously described in voltage-gated potassium and sodium channels (31), and that flows through the "omega pore" delineated by TM1–TM4. There is currently no evidence to support the existence of a second ion permeation pathway in TRPV1. Regardless, several observations lead us to believe that an omega pore equivalent to that identified in TRPM3 is not responsible for large cation selectivity. Both NMDG permeability and YO-PRO1 uptake via TRPV1 are drastically affected by alterations within the central pore domain, such as mutagenesis, the presence of pore blockers, and cysteine-modifying reagents (10). This is in stark contrast to the TRPM3 omega current, which is completely insensitive to pharmacological blockade and chemical modification of the central pore but is affected by mutations within TM4 (30). Furthermore, the omega pore is impermeable to NMDG, and opening of this pathway does not alter TRPM3 ionic selectivity.

Agonist-evoked changes in ion channel reversal potential have been interpreted by some investigators as being indicative of changes in ion selectivity (10, 14, 16, 32) and by others as an indirect result of ion flux-dependent dissipation of transmembrane gradients (33). In one recent study, it was demonstrated that TRPV1-dependent uptake of the large cation QX-314 is detectable at very early times after agonist addition and does lead to some intracellular accumulation of this ion (34). This finding is consistent with our observation of a basal level of NMDG permeability at the outset of the RTX- or capsaicin-evoked response. We certainly cannot exclude ion accumulation as a contributor to the changes in E_{rev} recorded in our experiments. It might, for example, provide one explanation for the sodium conductance-dependence of the E_{rev} shift. Similarly, as described above, NMDG block of sodium currents

could augment measured E_{rev} changes. Still, several observations suggest that ion accumulation and NMDG block alone cannot adequately explain our findings. First, multiple TRPV1 mutants exhibited abnormalities in maximal E_{rev} and ΔE_{rev}, despite sodium current densities and conductances that were either normal or altered in the opposite direction. Disproportionate changes in E_{rev} *versus* sodium current amplitudes were also previously observed following application of cysteine-modifying reagents in rTRPV1-M644C (10). Thus, the phenotypes we observed in this study are likely to reflect differences in ionic selectivity, *per se*, rather than being an indirect consequence of increases or decreases in general channel activity and ion accumulation. Second, the effect of a given phenotypic mutation on maximal or delta E_{rev} or P_{NMDG}/P_{Na} was typically far greater than that on minimal E_{rev} or P_{NMDG}/P_{Na}. In some cases, mutants exhibiting no significant differences from wild type in minimal values (rat G618W, N628P, and S629A; mouse N629P) exhibited substantial differences in maximal values during RTX exposure, supporting the existence of a dynamic component to large cation permeability. Our structural models also revealed differential impacts of mutations on apo- *versus* ligand-bound channel structures. Third, differences in the agonist-evoked increase in YO-PRO1 uptake rate among mutants largely corroborated our electrophysiological findings and in some cases provided a more sensitive measure of loss-of-function. Fourth, sodium conductance declined far less during RTX stimulation than did current at +20 mV, arguing against NMDG block as the major explanation for our findings. Fifth, comparison of cryo-EM-derived TRPV1 structures in the apo- or capsaicin-bound states *versus* the RTX/DkTx-bound state provides direct evidence that agonist activation can increase the diameter of the TRPV1 pore (3, 4).

Although substantial, the pore dilation measured in RTX/DkTx-bound TRPV1 was still not sufficient to account for TRPV1 permeability to the large cations used in this study. One possible explanation for this finding is that the RTX/DkTx-bound structure, like the capsaicin-bound channel, represents an intermediate state and that conformations exhibiting even greater pore expansion are transient and were therefore not captured in the cryo-electron microscopy studies. A second possibility is that large cations are themselves able to induce further expansion of a flexible TRPV1 selectivity filter as they pass through the activated channel. As pointed out by Liao *et al.* (3), TRPV1 pore flexibility is likely facilitated by the short length of, and lack of stabilizing hydrogen bonds within, the selectivity filter, compared with those of sodium and potassium channels whose pores exhibit more rigidity during gating. A third possibility, given that large cation selectivity was not assayed in the minimal TRPV1 construct used for the structural studies, is that partial deletion of the pore turret and C-terminal domains rendered the modified channel incapable of achieving full pore expansion. Indeed, our mutagenesis screen demonstrates that the pore turret domain contains several determinants of large cation permeability. Furthermore, we have observed that truncation of the TRPV1 C-terminal domain by 72 residues virtually eliminates capsaicin-induced changes in E_{rev} (data not shown).

Throughout our study, mutants exhibiting enhanced large cation permeability were far more prevalent than those displaying a selective loss of this capacity, and those few loss-of-function mutants that we did identify exhibited only partial deficits. It is possible that some more robust loss-of-function phenotypes were masked by virtue of mutant channels having pores so narrow or inflexible that sodium current was also impeded. This interpretation is supported by the relatively constricted nature of the apo-TRPV1 upper pore (3). If, as suggested, the reported capsaicin-bound TRPV1 conformation represents an incompletely gated channel (4), some of our mutants demonstrating an overall functional deficit may have become trapped in this conformation and unable to undergo further activation.

Whereas our data are most simply interpreted in the context of changes in physical pore diameter, this represents only one way in which alterations in large cation permeability might arise. For example, hydrogen bonding interactions between pore residues and permeating cations or alterations in dehydration of ions entering the pore might also change with persistent agonist activation, and these effects might be altered by the mutations we introduced. We also cannot exclude the possibility that, in some mutant channels, NMDG may be differentially effective at occluding the pore, diminishing sodium efflux to an extent distinct from that seen in wild type TRPV1.

Our data provide insight into potential interactions between the sequence determinants of ionic selectivity. Notably, the effects of the M644I mutation could be countered by the gain-of-function N628P mutation, as evident in both the NMDG and YO-PRO1 assays. Meanwhile, combination of two gain-of-function substitutions, N628P and M644A, did not produce additive effects. This may signify that the M644A mutant achieves the maximal pore dilation or flexibility compatible with channel function or stability. In contrast, loss-of-function mutations (G618W and M644I) did produce apparently additive effects, although this was only evident from examination of YO-PRO1 uptake. Together, these findings suggest that even sites at a distance from the selectivity filter can alter its static and dynamic properties. Interactions between the selectivity filter and adjacent domains are crucial determinants of C-type inactivation and ionic selectivity in potassium channels (35–39). Alkaline pH has been shown to cause functional "dilation" of the pore of TRPV5 through mechanisms apparently involving the pore helix (40). Furthermore, the selectivity filter and surrounding residues are critical for gating of TRPV1 by heat, protons, cations, and toxins such as DkTx (21, 41–46). Our findings provide further support for this concept.

Our data revealed a differential effect of the M644A substitution on YO-PRO1 uptake evoked by RTX *versus* capsaicin. As discussed above, although a structure of TRPV1 occupied by RTX alone has not yet been reported, there were substantial disparities in conformational changes induced by capsaicin *versus* the RTX/DkTx combination, including differential effects on the selectivity filter and opposing rotations of the Ile-679 residue in the lower pore gate (4). A similar theme recently emerged from the finding that heat and capsaicin exert different conformational effects at the rat TRPV1-Y653 residue (21, 47). Moreover, capsaicin and RTX were previously shown to differentially alter TRPV1 calcium permeability (10) and to

evoke disparate single channel behaviors in TRPV1 (27). Together, these findings support the notion that TRPV1 gating can be qualitatively heterogeneous, even among similar agonists.

Previous studies of the ATP-gated $P2X_2$ channel (48, 49) and, more recently, TRPV1 itself (28) have suggested that desensitization (calcium-dependent desensitization, in the case of TRPV1) and dynamic permeability represent tightly linked phenomena. We did not observe a clear relationship between TRPV1-mediated sodium current kinetics and dynamic large cation permeability in this study. However, our experiments were performed in the absence of extracellular calcium ions. In future studies, it would therefore be interesting to evaluate calcium-dependent desensitization kinetics in the mutants described here. It would also be of value to determine how these mutations influence large cation permeability changes evoked by non-vanilloid TRPV1 agonists and how they affect agonist-evoked changes in permeability to more physiologically relevant ions, such as calcium. Single channel characterization of the ionic selectivity mutants identified in this study, coupled with direct structural analysis, might provide valuable insights into the conformational changes in the TRPV1 pore that permit large cation permeability. Finally, the *in vivo* substitution of phenotypic mutants for endogenous TRPV1 in sensory neurons might facilitate an understanding of the physiological importance of dynamic ion selectivity. Based on what we have learned to date, however, we conclude that side chain interactions at a few specific loci within the TRPV1 pore contribute to the dynamic process of ionic selectivity.

Acknowledgments—We thank Beata Durcanova, Queenie Qiu, and Juan Wang for assistance with site-directed mutagenesis; David Yue (Johns Hopkins University) for assistance with quantitative analysis; Jorg Grandl (Duke University), Sung Eun Kim, and Ardem Patapoutian (Scripps Research Institute) for sharing Asn-628 mutants; and members of the Caterina laboratory for helpful discussions.

REFERENCES

1. Caterina, M. J., Schumacher, M. A., Tominaga, M., Rosen, T. A., Levine, J. D., and Julius, D. (1997) The capsaicin receptor: a heat-activated ion channel in the pain pathway. *Nature* **389,** 816–824
2. Caterina, M. J., and Julius, D. (2001) The vanilloid receptor: a molecular gateway to the pain pathway. *Annu. Rev. Neurosci.* **24,** 487–517
3. Liao, M., Cao, E., Julius, D., and Cheng, Y. (2013) Structure of the TRPV1 ion channel determined by electron microscopy. *Nature* **504,** 107–112
4. Cao, E., Liao, M., Cheng, Y., and Julius, D. (2013) TRPV1 structures in distinct conformations reveal activation mechanisms. *Nature* **504,** 113–118
5. Meyers, J. R., MacDonald, R. B., Duggan, A., Lenzi, D., Standaert, D. G., Corwin, J. T., and Corey, D. P. (2003) Lighting up the senses: FM1–43 loading of sensory cells through nonselective ion channels. *J. Neurosci.* **23,** 4054–4065
6. Hellwig, N., Plant, T. D., Janson, W., Schäfer, M., Schultz, G., and Schaefer, M. (2004) TRPV1 acts as proton channel to induce acidification in nociceptive neurons. *J. Biol. Chem.* **279,** 34553–34561
7. Myrdal, S. E., and Steyger, P. S. (2005) TRPV1 regulators mediate gentamicin penetration of cultured kidney cells. *Hear. Res.* **204,** 170–182
8. Ahern, G. P., Wang, X., and Miyares, R. L. (2006) Polyamines are potent ligands for the capsaicin receptor TRPV1. *J. Biol. Chem.* **281,** 8991–8995
9. Binshtok, A. M., Bean, B. P., and Woolf, C. J. (2007) Inhibition of nociceptors by TRPV1-mediated entry of impermeant sodium channel blockers. *Nature* **449,** 607–610
10. Chung, M. K., Güler, A. D., and Caterina, M. J. (2008) TRPV1 shows dynamic ionic selectivity during agonist stimulation. *Nat. Neurosci.* **11,** 555–564
11. Chung, M. K., Güler, A. D., and Caterina, M. J. (2005) Biphasic currents evoked by chemical or thermal activation of the heat-gated ion channel, TRPV3. *J. Biol. Chem.* **280,** 15928–15941
12. Chen, J., Kim, D., Bianchi, B. R., Cavanaugh, E. J., Faltynek, C. R., Kym, P. R., and Reilly, R. M. (2009) Pore dilation occurs in TRPA1 but not in TRPM8 channels. *Mol. Pain* **5,** 3
13. Banke, T. G., Chaplan, S. R., and Wickenden, A. D. (2010) Dynamic changes in the TRPA1 selectivity filter lead to progressive but reversible pore dilation. *Am. J. Physiol. Cell Physiol.* **298,** C1457–C1468
14. Karashima, Y., Prenen, J., Talavera, K., Janssens, A., Voets, T., and Nilius, B. (2010) Agonist-induced changes in Ca^{2+} permeation through the nociceptor cation channel TRPA1. *Biophys. J.* **98,** 773–783
15. Surprenant, A., Rassendren, F., Kawashima, E., North, R. A., and Buell, G. (1996) The cytolytic P2Z receptor for extracellular ATP identified as a P2X receptor (P2X7). *Science* **272,** 735–738
16. Khakh, B. S., Bao, X. R., Labarca, C., and Lester, H. A. (1999) Neuronal P2X transmitter-gated cation channels change their ion selectivity in seconds. *Nat. Neurosci.* **2,** 322–330
17. Virginio, C., MacKenzie, A., Rassendren, F. A., North, R. A., and Surprenant, A. (1999a) Pore dilation of neuronal P2X receptor channels. *Nat. Neurosci.* **2,** 315–321
18. Virginio, C., MacKenzie, A., North, R. A., and Surprenant, A. (1999b) Kinetics of cell lysis, dye uptake and permeability changes in cells expressing the rat P2X7 receptor. *J. Physiol.* **519,** 335–346
19. Jiang, L. H., Rassendren, F., Mackenzie, A., Zhang, Y. H., Surprenant, A., and North, R. A. (2005) *N*-Methyl-D-glucamine and propidium dyes utilize different permeation pathways at rat P2X(7) receptors. *Am. J. Physiol. Cell Physiol.* **289,** C1295–C1302
20. Kaczmarek-Hájek, K., Lörinczi, E., Hausmann, R., and Nicke, A. (2012) Molecular and functional properties of P2X receptors–recent progress and persisting challenges. *Purinergic Signal.* **8,** 375–417
21. Grandl, J., Kim, S. E., Uzzell, V., Bursulaya, B., Petrus, M., Bandell, M., and Patapoutian, A. (2010) Temperature-induced opening of TRPV1 ion channel is stabilized by the pore domain. *Nat. Neurosci.* **13,** 708–714
22. Tominaga, M., Caterina, M. J., Malmberg, A. B., Rosen, T. A., Gilbert, H., Skinner, K., Raumann, B. E., Basbaum, A. I., and Julius, D. (1998) The cloned capsaicin receptor integrates multiple pain-producing stimuli. *Neuron* **21,** 531–543
23. Brooks, B. R., Brooks, C. L., 3rd, Mackerell, A. D., Jr., Nilsson, L., Petrella, R. J., Roux, B., Won, Y., Archontis, G., Bartels, C., Boresch, S., Caflisch, A., Caves, L., Cui, Q., Dinner, A. R., Feig, M., Fischer, S., Gao, J., Hodoscek, M., Im, W., Kuczera, K., Lazaridis, T., Ma, J., Ovchinnikov, V., Paci, E., Pastor, R. W., Post, C. B., Pu, J. Z., Schaefer, M., Tidor, B., Venable, R. M., Woodcock, H. L., Wu, X., Yang, W., York, D. M., and Karplus, M. (2009) CHARMM: the biomolecular simulation program. *J. Comput. Chem.* **30,** 1545–1614
24. Eickhorst, A. N., Berson, A., Cockayne, D., Lester, H. A., and Khakh, B. S. (2002) Control of P2X(2) channel permeability by the cytosolic domain. *J. Gen. Physiol.* **120,** 119–131
25. Fujiwara, Y., and Kubo, Y. (2004) Density-dependent changes of the pore properties of the P2X2 receptor channel. *J. Physiol.* **558,** 31–43
26. Yang, F., Cui, Y., Wang, K., and Zheng, J. (2010) Thermosensitive TRP channel pore turret is part of the temperature activation pathway. *Proc. Natl. Acad. Sci. U.S.A.* **107,** 7083–7088 ***20351268***
27. Raisinghani, M., Pabbidi, R. M., and Premkumar, L. S. (2005) Activation of transient receptor potential vanilloid 1 (TRPV1) by resiniferatoxin. *J. Physiol.* **567,** 771–786
28. Veldhuis, N. A., Lew, M. J., Abogadie, F. C., Poole, D. P., Jennings, E. A., Ivanusic, J. J., Eilers, H., Bunnett, N. W., and McIntyre, P. (2012) *N*-Glycosylation determines ionic permeability and desensitization of the TRPV1 capsaicin receptor. *J. Biol. Chem.* **287,** 21765–21772
29. García-Martínez, C., Morenilla-Palao, C., Planells-Cases, R., Merino, J. M., and Ferrer-Montiel, A. (2000) Identification of an aspartic residue in the P-loop of the vanilloid receptor that modulates pore properties. *J. Biol.*

Chem. **275,** 32552–32558
30. Vriens, J., Held, K., Janssens, A., Tóth, B. I., Kerselaers, S., Nilius, B., Vennekens, R., and Voets, T. (2014) Opening of an alternative ion permeation pathway in a nociceptor TRP channel. *Nat. Chem. Biol.* **10,** 188–195
31. Tombola, F., Pathak, M. M., Gorostiza, P., and Isacoff, E. Y. (2007) The twisted ion-permeation pathway of a resting voltage-sensing domain. *Nature* **445,** 546–549
32. Jansson, E. T., Trkulja, C. L., Ahemaiti, A., Millingen, M., Jeffries, G. D., Jardemark, K., and Orwar, O. (2013) Effect of cholesterol depletion on the pore dilation of TRPV1. *Mol. Pain* **9,** 1
33. Ferrini, F., Trang, T., Mattioli, T. A., Laffray, S., Del'Guidice, T., Lorenzo, L. E., Castonguay, A., Doyon, N., Zhang, W., Godin, A. G., Mohr, D., Beggs, S., Vandal, K., Beaulieu, J. M., Cahill, C. M., Salter, M. W., and De Koninck, Y. (2013) Morphine hyperalgesia gated through microglia-mediated disruption of neuronal Cl^- homeostasis. *Nat. Neurosci.* **16,** 183–192
34. Puopolo, M., Binshtok, A. M., Yao, G. L., Oh, S. B., Woolf, C. J., and Bean, B. P. (2013) Permeation and block of TRPV1 channels by the cationic lidocaine derivative QX-314. *J. Neurophysiol.* **109,** 1704–1712
35. Doyle, D. A., Morais Cabral, J., Pfuetzner, R. A., Kuo, A., Gulbis, J. M., Cohen, S. L., Chait, B. T., and MacKinnon, R. (1998) The structure of the potassium channel: molecular basis of K^+ conduction and selectivity. *Science* **280,** 69–77
36. Cordero-Morales, J. F., Jogini, V., Lewis, A., Vásquez, V., Cortes, D. M., Roux, B., and Perozo, E. (2007) Molecular driving forces determining potassium channel slow inactivation. *Nat. Struct. Mol. Biol.* **14,** 1062–1069
37. Lees-Miller, J. P., Subbotina, J. O., Guo, J., Yarov-Yarovoy, V., Noskov, S. Y., and Duff, H. J. (2009) Interactions of H562 in the S5 helix with T618 and S621 in the pore helix are important determinants of hERG1 potassium channel structure and function. *Biophys. J.* **96,** 3600–3610
38. Wang, Z., Wong, N. C., Cheng, Y., Kehl, S. J., and Fedida, D. (2009) Control of voltage-gated K^+ channel permeability to $NMDG^+$ by a residue at the outer pore. *J. Gen. Physiol.* **133,** 361–374
39. Chao, C. C., Huang, C. C., Kuo, C. S., and Leung, Y. M. (2010) Control of ionic selectivity by a pore helix residue in the Kv1.2 channel. *J. Physiol. Sci.* **60,** 441–446
40. Yeh, B. I., Kim, Y. K., Jabbar, W., and Huang, C. L. (2005) Conformational changes of pore helix coupled to gating of TRPV5 by protons. *EMBO J.* **24,** 3224–3234
41. Myers, B. R., Bohlen, C. J., and Julius, D. (2008) A yeast genetic screen reveals a critical role for the pore helix domain in TRP channel gating. *Neuron* **58,** 362–373
42. Cui, Y., Yang, F., Cao, X., Yarov-Yarovoy, V., Wang, K., and Zheng, J. (2012) Selective disruption of high sensitivity heat activation but not capsaicin activation of TRPV1 channels by pore turret mutations. *J. Gen. Physiol.* **139,** 273–283
43. Ryu, S., Liu, B., Yao, J., Fu, Q., and Qin, F. (2007) Uncoupling proton activation of vanilloid receptor TRPV1. *J. Neurosci.* **27,** 12797–12807
44. Aneiros, E., Cao, L., Papakosta, M., Stevens, E. B., Phillips, S., and Grimm, C. (2011) The biophysical and molecular basis of TRPV1 proton gating. *EMBO J.* **30,** 994–1002
45. Ahern, G. P., Brooks, I. M., Miyares, R. L., and Wang, X. B. (2005) Extracellular cations sensitize and gate capsaicin receptor TRPV1 modulating pain signaling. *J. Neurosci.* **25,** 5109–5116
46. Bohlen, C. J., Priel, A., Zhou, S., King, D., Siemens, J., and Julius, D. (2010) A bivalent tarantula toxin activates the capsaicin receptor, TRPV1, by targeting the outer pore domain. *Cell* **141,** 834–845
47. Kim, S. E., Patapoutian, A., and Grandl, J. (2013) Single residues in the outer pore of TRPV1 and TRPV3 have temperature-dependent conformations. *PLoS One* **8,** e59593
48. Fisher, J. A., Girdler, G., and Khakh, B. S. (2004) Time-resolved measurement of state-specific P2X2 ion channel cytosolic gating motions. *J. Neurosci.* **24,** 10475–10487
49. Khakh, B. S., and Egan, T. M. (2005) Contribution of transmembrane regions to ATP-gated P2X2 channel permeability dynamics. *J. Biol. Chem.* **280,** 6118–6129